ELECTRON-CAPTURES IN SUPERNOVAE

By

LeShawna Valdez

A THESIS

Submitted to
Michigan State University
in partial fulfillment of the requirements
for the degree of

MASTER OF SCIENCE

Physics

2012

ABSTRACT

ELECTRON-CAPTURES IN SUPERNOVAE

By

LeShawna Valdez

A method to effectively compare electron-capture rates calculated from both theoretical and experimental Gamow-Teller strength distributions has been created. In this thesis, the method has been outlined and applied to the transition from ^{56}Fe to ^{56}Mn. Factors that significantly impact the electron-capture rates are the stellar temperature, the stellar density, the excitation energy spectrum of the daughter nucleus, and the strength of the Gamow-Teller transitions. The ability of theoretical models to reproduce the locations (and to a lesser degree, the strengths) of the low-lying states that can be captured into, is the most crucial factor in producing reliable electron-capture rates. A good agreement was found between Gamow-Teller transitions calculated using the GXPF1a interaction in the shell-model and the recent data from a high resolution ^{56}Fe$(t,^3$He$)$ experiment. Since calculations with the KB3G interaction, which forms the basis for a weak reaction-rate library commonly used in astrophysical simulations do worse, it is suggested that improvements can be made to the current inputs for astrophysical models. This conclusion is in agreement with recent results from a ^{56}Ni(p,n) experiment where experimental Gamow-Teller strengths from ^{56}Ni were compared with theory. The procedure outlined in this thesis can be used to further constrain theoretical Gamow-Teller strength calculations with new, successfully developed charge-exchange probes which will be utilized at rare isotope beam facilities such as FRIB.

ACKNOWLEDGMENTS

iv

guidance and research experience: Rich Lebed and Ricardo Alarcon. Rich, thank you for being such a good friend, mentor, and teacher. Ricardo, thank you for giving me such good advice and for the opportunity to work with you. I also want to thank my many friends at NSCL and BPS who provided me with laughs and fun trips on Mondays to the Dairy Store for the grilled cheese-tomato soup combo without which the week would never be the same. Last but definitely not least, my family for their never-ending encouragement.

TABLE OF CONTENTS

LIST OF FIGURES

Chapter 1

Introduction and Motivation

1.1 Supernovae

Interstellar clouds of gas and dust form the birthing region for stars. Compression of this gas and dust due to gravity creates a protostar and as this protostar continues to contract, the temperature and density increase. At low temperatures, the hydrogen nuclei repel each as a result of Coulomb repulsion. However, if the nuclei were to get close enough the strong nuclear force would take over and the nuclei would attract. An increase in temperature provides the energy needed for this attraction to begin. As the temperature increases, kinetic energy increases eventually becoming greater than the coulomb barrier. The hydrogen nuclei now have enough energy to overcome this barrier and attract one another leading to fusion of nuclei. It is at this point that the star begins its life on the main sequence where it will spend most of its life forming helium through hydrogen fusion [1]. Stars can fuse higher mass nuclei and stars whose mass $M \gtrsim 8 M_\odot$ continue consuming heavier elements until the most massive stars form a core of "iron-group" of nuclei through silicon burning. The members of

the "iron-group" dominating the late stellar core consist of ^{54}Fe, ^{56}Fe, and ^{56}Ni [1]. These nuclei have the highest binding energy per nucleon of all other nuclei with ^{62}Ni having the greatest. Reaching the "iron-group" means the end of nuclear fusion in the core of the star since fusing iron would take away energy rather than provide it. This eventually sends the star into the core-collapse supernova phase which is to be discussed in section 1.1.1. Stars less massive than those ending their lives in core-collapse supernovae evolve off the main sequence forming red giants and eventually white dwarfs. It is possible for these stars to end their lives in explosions as well and is the topic of section 1.1.2. Both types of explosions are important in that they are major sources of heavy elements in the universe.

It has taken centuries for observers to realize the importance of these catastrophic events. The earliest record of such an event was labeled a "guest star" by ancient Chinese observers [2]. Centuries later, the term "nova" was introduced by Tycho Brahe with the publication of his book *De Nova Stella* meaning *Of the New Star*, after observing the supernova that now bears his name in 1572 [3]. In the 1930s, Fritz Zwicky introduced the term "super-novae" to distinguish from more common novae. He, along with Walter Baade were the first to define categories for these appearances: common novae, and super-novae [4]. Today, supernovae themselves have been further categorized into two types, those containing hydrogen lines being Type II and those without, Type I [3]. Subcategories are contained within the two types but an important distinction is that Type Ia supernovae are thermonuclear while all others are core-collapse supernovae. Although the exact dynamics of the explosion are not well understood for either events, it has become clear that weak reactions, electron-capture (EC) in particular, play an important role [5]. To understand EC's role in supernovae dynamics, it is important to first address the types of supernovae.

1.1.1 Core-Collapse Supernovae

Core-collapse supernovae take place in high mass stars ($M \gtrsim 8M_\odot$) after the star has used up its nuclear fuel for fusion in the core. At this point, thermal pressure is no longer supporting the weight of the outer layers and electron-degeneracy pressure supports the star.

It has been shown that the maximum mass the degenerate core is able to withstand is directly proportional to the square of the fraction of electrons in the core $M_{CH} \propto Y_e^2$ [6]. Under $T \sim 10^9$ K and $\rho Y_e \sim 10^7 - 10^9$ g·cm^{-3} stellar conditions, ECs begin to take place in high number thereby reducing the amount of weight electron-degeneracy pressure can support and the layers fall inward. This increases the density allowing more ECs to take place, reducing the electron-degeneracy pressure and the layers fall inward once again. This process continues until nuclear density is reached. At this point, the core rebounds and the shock wave is initialized leading to the explosion of the star. The remnant of a core-collapse supernova (SN 1987a) is shown in figure 1.1.
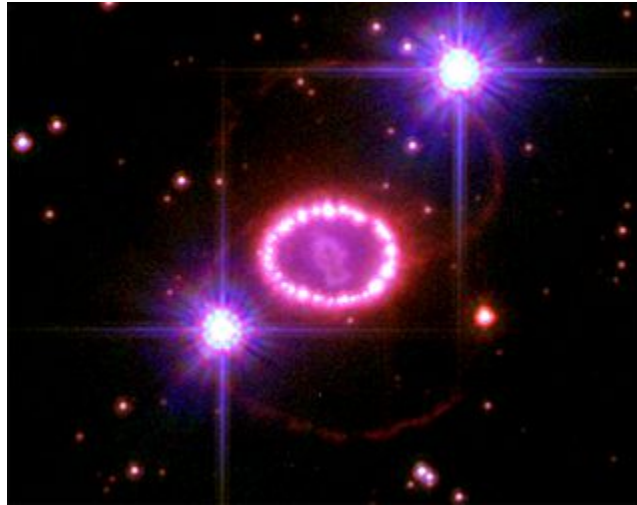
Figure 1.1: The remnant of supernova 1987a. Courtesy Space Telescope Science Institute/NASA [7]. For interpretation of the references to color in this and all other figures, the reader is referred to the electronic version of this thesis.

During the pre- and post-collapse phases, ECs take place on a variety of $pf-$ and $sdg-$shell nuclei [8], many of which under terrestrial conditions are unstable. Moreover, due to the high temperature ECs can take place on the thermally populated excited states. Measuring all the relevant EC rates in this region would be impossible. This is particularly due to the vast number of experiments it would involve and the impossibility of studying the transition from excited states. Hence, it is crucial that theoretical models are developed and tested against experiment [5].

1.1.2   Thermonuclear Supernovae

Although thermonuclear supernovae serve as "standard candles" in astronomy for determining cosmic distances due to the similarity of their light curves [1], they are even less well understood than core-collapse supernovae. The current general hypothesis is that these supernovae begin in binary star systems. Two progenitors have been suggested: two white dwarfs that merge or a white dwarf and an accompanying red giant that accretes mass on the dwarf [9]. The resulting explosion is similar in each case.

Stars that are $0.5M_\odot \lesssim M \lesssim 8M_\odot$ end up as white dwarfs. Fusion has ended in the core and electron degeneracy pressure is left to support the star. As the mass of the dwarf increases - either by accretion from a red giant or from a merger with another dwarf - the temperature, pressure, and density increase. Slightly before the white dwarf nears the Chandrasekhar limit of approximately $1.4M_\odot$, carbon fusion is ignited in the core. Main sequence stars are able to expand in order to control temperature and fusion; however, as a dwarf is in a degenerate state it cannot expand. Therefore as fusion is ignited in the core, a deflagration front quickly moves to the surface. As it does so it converts about half of the mass to iron.

Figure 1.2: This is the remnant of the supernova spotted by Tycho Brahe in 1572. Here, it is shown in the infrared and X-ray and was photographed using NASA's Spitzer and Chandra observatories. SN1572 left behind a nebula type remnant that does not contain a neutron star. Courtesy NASA/JPL-Caltech [11].

ECs take place on these nuclei, the degeneracy is lifted, and the dwarf quickly expands. This provides enough energy to throw the star out of stability and finally, into an explosion. Type Ia supernovae leave remnants in their wake such as that left by SN 1572, known as Tycho's supernova shown in figure 1.2.

ECs are an important contributor to thermonuclear supernova models. These ECs depend both on the velocity of the deflagration front and the central density of the dwarf [10]. Since ECs are taking place on the iron nuclei that were formed in the burning front, they also affect the resultant nucleosynthesis. Therefore, knowing this resultant nucleosynthesis and knowing accurate EC rates allow for important constraints on the central density and the velocity of the flame front in supernova models [10]. Similar to the case of Type II, models that generate EC rates must be tested against experiment for accuracy.

1.2 Electron-Capture and Charge-Exchange

During the EC process, an electron is captured by a proton in the nucleus forming a neutron and releasing a neutrino. A diagram of this process is shown in figure 1.3. Charge-exchange (CE) is an analogous reaction mediated by the strong force that connects the same initial and final states as EC ($\Delta L = 0, \Delta S = 1$) [12]. Therefore, the Gamow-Teller (GT) transition strengths obtained from a CE experiment can be used as inputs into EC rate calculations. An advantage of using CE to probe GT transition strengths to daughter excitation energies is that it can probe to higher excitation energy since it is not limited by Q-value. Initially, supernovae were believed to be insensitive to details of the EC rates and the associated GT distributions. This was shown by Bethe et. al. [13] when applied to extreme conditions of the collapse phase. However, when Fuller et. al. [14] applied EC rates to the less extreme phases such as pre- and post-collapse, they determined that the weak reaction rates, in fact, greatly affect the dynamics.

Determining weak reaction rates for masses relevant to these phases of the supernovae was the goal of a series of papers published by Fuller, Fowler, and Newman [14–17]. Although the GT strength distributions that serve as inputs for these calculations turned out to be too simple and more realistic models are now in use, their work formed the basis for the techniques applied in modern simulations. There are two important factors in EC rate calculations:

- GT strengths of the transition and
- phase space.

As mentioned before, the GT strengths calculated by theoretical models must be tested against experiment. CE experiments are the preferred tool for that purpose. It is important

(a) Charge-Exchange Reaction   (b) Electron-Capture
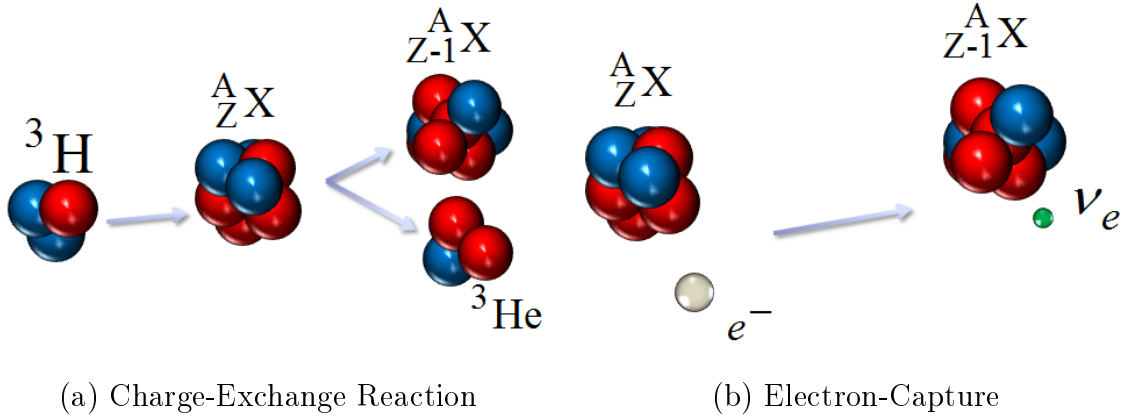
Figure 1.3: electron-capture is a weak reaction analogous to charge-exchange which is mediated by the strong force. The initial and final states are the same in each reaction enabling the use of charge-exchange to extract the Gamow-Teller strengths in electron-capture. a) A triton is impinged on a target. A neutron is then exchanged for a proton resulting in the release of ^{3}He with a left over nucleus with less one proton but same mass number. b) An electron is captured by a nucleus changing the proton number and releasing a neutrino.

to note that the CE experiments probe transitions to excited states in a daughter nucleus from the ground state of the parent nucleus as shown in figure 1.4. An EC rate can be determined for each of these individual transitions with the total rate being the sum of the individual rates.

$$\lambda = \Sigma_{ij}\lambda_{ij}. \tag{1.1}$$

The parent and daughter states are i and j, respectively. These individual rates are determined from [14],

$$\lambda_{ij} = \ln 2 \frac{f_{ij}(T, \rho, U_F)}{(ft)_{ij}}. \tag{1.2}$$

Here the half-life, $(ft)_{ij}$, is related to the nuclear matrix elements of a weak nuclear interaction,

$$B(F) + \left(\frac{g_A}{g_V}\right)^2 B_{ij}(GT) = \frac{K/g_V^2}{(ft)_{ij}}. \tag{1.3}$$

7
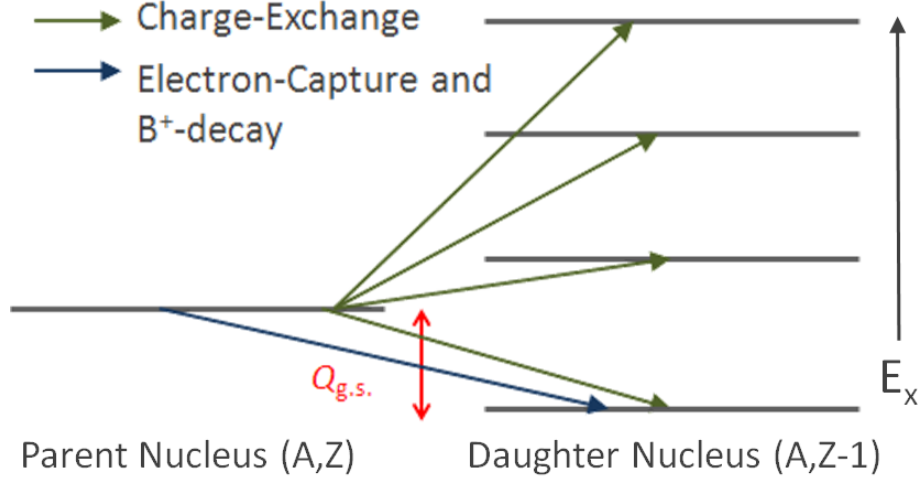
Figure 1.4: In an experiment, daughter states are probed using a charge-exchange reaction. The difference in the ground state of the mother nucleus and daughter nucleus is $Q_{g.s.}$.

The weak decay vector and axial-vector coupling constants, g_V and g_A, are related via $\frac{g_A}{g_V} = -1.2694 \pm 0.0028$ and $K/g_V^2 = 6143 \pm 2$ s [18]. For pure Gamow-Teller transitions, $B(F) = 0$ and the half life becomes,

$$ft = \frac{3812s}{B_{ij}(GT)}. \tag{1.4}$$

The individual rates depend on the temperature of the star (T), the density (ρ), and the electron chemical potential (U_F) through the phase space integral f_{ij} used for calculating electron-capture rates. For electrons it takes the form [14],

$$f_{ij}(T, \rho, U_F) = \int_{w_l}^{\infty} w^2 (q_R + w)^2 S_-(T, U_F(\rho)) dw \tag{1.5}$$

with the total energy of the electron being ε_e and $w = \varepsilon_e/m_e c^2$. The EC threshold total energy is $w_l = |q_{g.s.}|$ with $q_{g.s.} = Q_{g.s.}/m_e c^2$. Here $Q_{g.s.} = m_N(^A_Z X) - m_N(^A_{Z-1} X) - m_e c^2$ and m_N referres to nuclear mass excess. The Q-value of the reaction in units of

electron mass is [19]:

$$q_R = Q_R/m_e c^2 = \left[E_{xj} - E_{xi} - Q_{g.s}\right]/m_e c^2 \qquad (1.6)$$

Finally, the term

$$S_- = \left(\exp\left(\frac{U - U_F}{kT}\right) + 1\right)^{-1} \qquad (1.7)$$

is the Fermi-Dirac distribution function. In the distribution function, the kinetic energy is $U = (w-1)m_e c^2$ and k is the Boltzmann constant. At zero temperature, the chemical potential is approximated by [14, 20],

$$U_F = 0.511\text{MeV}\left[\left(1.018\,(\rho_6 Y_e)^{2/3} + 1\right)^{1/2} - 1\right] \qquad (1.8)$$

where ρ_6 is the density ρ divided by 10^6g/cm^3 and Y_e is the electron fraction. The Fermi energy is $\varepsilon_F = U_F + m_e c^2$ and a plot of ε_F as a function of density is shown in figure 1.5. In order for EC to take place, $\varepsilon_F > Q_R$. Finally, putting these factors together and setting $(i = 1)$ since the parent nucleus is in the ground state the EC rates can be calculated with the equation:

$$\lambda_{g.s.} = \sum_j \frac{B_{1j}(GT)}{6182s} \int_{w_l}^{\infty} w^2 (q_R + w)^2 \left(\exp\left(\frac{U - U_F}{kT}\right) + 1\right)^{-1}. \qquad (1.9)$$

EC rate calculations are complicated by the extreme conditions present in the pre- and post-supernova phases and these factors will be discussed in the following section.
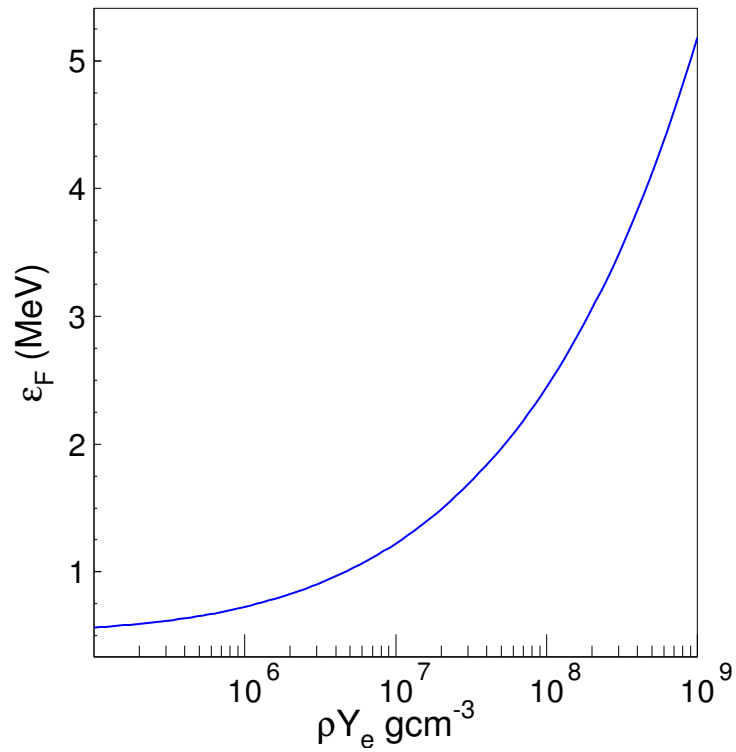
Figure 1.5: For electron-capture to take place in a star, the Fermi energy must be greater than the Q-value of the reaction. This plot is shown for zero temperature. At higher densities, the Fermi energy is higher, so transitions to higher excitation energies can contribute to the electron-capture rate.

1.3   Factors in Electron-Capture Rate Calculations

In this section, the main factors that affect the EC rates in the stellar environment will be discussed.

- Temperature in the star

- Density in the star

- Excitation energy of daughter nuclei relative to Fermi energy

- Gamow-Teller transition strength.

1.3.1   Temperature and Density of the Star

A pre-supernova star is at a temperature of $T \sim 10^9$ K. At low temperature ($T \lesssim 10^9$ K) the core is in a highly degenerate state, therefore all the electrons are in the lowest energy state they can possibly occupy without violating Pauli's exclusion principle. As temperature is increased, electrons are given thermal energy and begin to occupy higher energy states, thereby lifting the degeneracy. This is visualized with an artificially created GT spectrum shown in figure 1.6(a). To create this figure, B(GT) for each transition was set to unity with the ground state Q-value set to zero. The placements for each GT transition strength were $E_x = 1.5$, 2.0, 2.5, and 3.0 MeV. EC rate calculations were performed with each transition separately, i.e. assuming only one GT transition was active at a time. The result of each calculation is shown in figure 1.6(b) where the logarithm of the EC rate is plotted against stellar temperature (10^9 K). At low temperatures, the Fermi surface resides at the highest electron energy occupied by a degenerate electron as indicated by the dashed red line. This Fermi energy is a function of stellar density as shown in equation 1.2. As the temperature is increased, the Fermi surface smears out and higher excitation energies can start to contribute to EC as decribed schematically by the black curve.
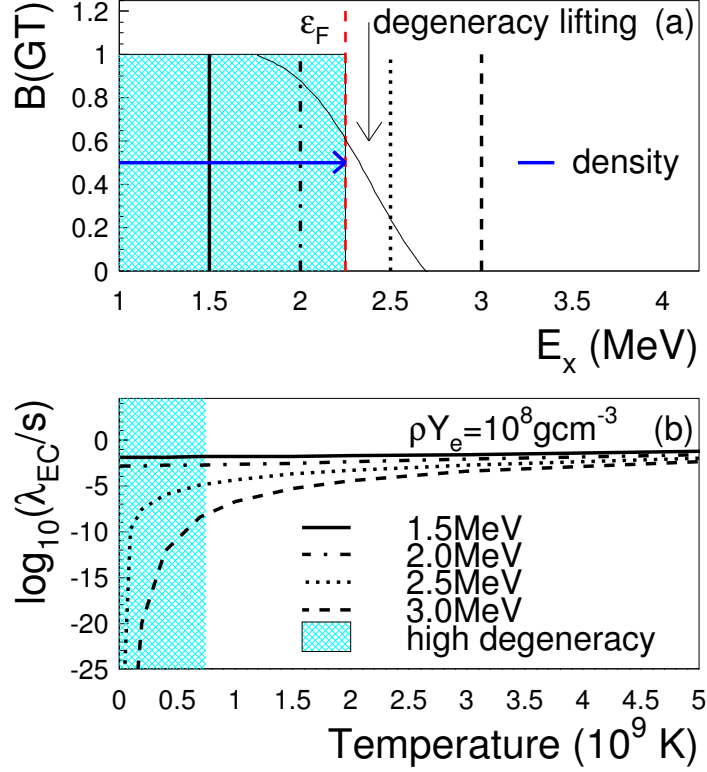
Figure 1.6: (a) An artificially created B(GT) spectrum with four states at E_x =1.5 MeV, 2.0 MeV, 2.5 MeV, and 3.0 MeV and B(GT)=1 for all states. At $\rho Y_e = 10^8$ g·cm^{-3} and low temperature the Fermi surface resides just above the 2 MeV level and a red dotted line was placed at this energy to approximate which excitations are above and below the Fermi energy. As temperature is increased the degeneracy is lifted. This is represented schematically with the solid black line in order to visualize the effect of degeneracy lifting. (b) The logarithm of the electron-capture rates as a function of temperature for $\rho Y_e = 10^8$ g·cm^{-3} for captures into each of the states in (a). When the electron gas is degenerate, only states below the Fermi surface have significant rates. At higher temperatures, electron-captures to states above the Fermi energy start to contribute.

Captures into excited states that are above the Fermi surface (2.5 MeV and 3.0 MeV) will contribute when the temperature is high enough to lift the degeneracy to a level of which electrons are available to capture into those states. Captures into the 2.5 MeV level will contribute significantly at lower temperatures than those into the 3.0 MeV level. For states below the Fermi surface (1.5 MeV and 2.0 MeV) the increase in temperature hardly affects

12
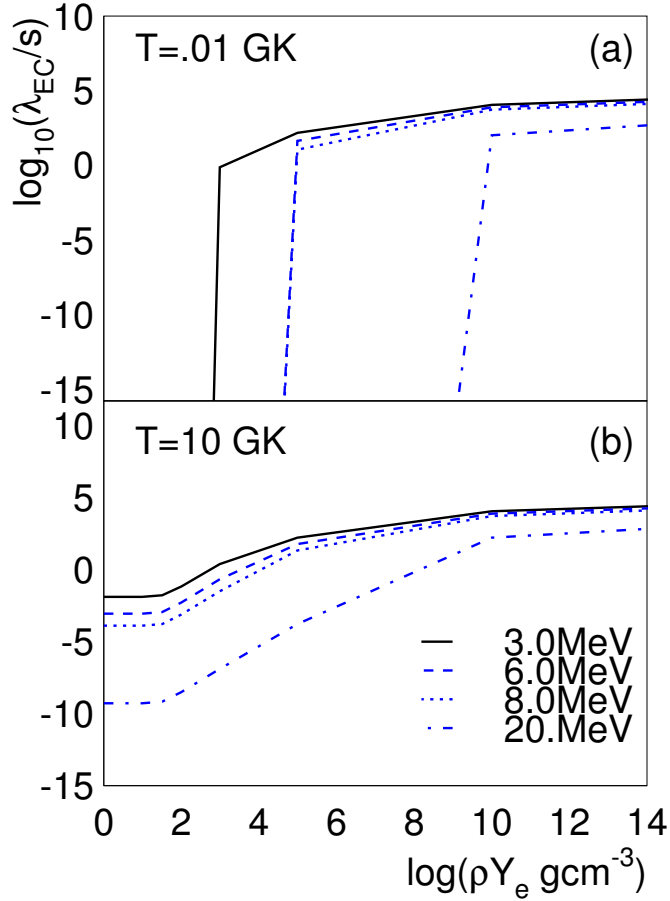
Figure 1.7: Electron-capture rates were calculated for a constant B(GT)=1 and $Q_{g.s} = 0$ MeV. The logarithm of the electron-capture rate was plotted against the logarithm of ρY_e for (a) $T = .01$ GK and (b) $T = 10$ GK. In the former case, the Fermi energy does not exceed excitation energy until a sufficient increase in ρY_e. Once $\varepsilon_F > E_x$ (with $Q_{g.s.} = 0$ MeV) there is a sharp increase in rates which occurs at higher ρY_e for higher excitation energies. When degeneracy has been lifted substantially at $T = 10$ GK, the Fermi surface is quite smeared out and all excitation energies are contributing to electron-capture, even at low ρY_e. 3 MeV is shown as a solid green line and is the same energy that is used in figure 1.9.

the associated EC rates. At sufficiently high temperature, differences in excitation energy and Fermi energy are less noticeable due to the considerable amount of lifted degeneracy.

As previously mentioned, at low temperature the electrons are in a highly degenerate state. As ρY_e in the star increases, the Fermi energy increases; therefore, EC to highly excited states can contribute. This effect is visualized in figure 1.6(a) in the cyan shaded

region. As ρY_e increases, captures can take place into excitation energies that were once above the Fermi energy. When ρY_e increases, the Fermi energy increases allowing captures into the state at 2.5 MeV to contribute. A further increase in ρY_e would increase the Fermi energy enough to allow captures into 3.0 MeV to finally contribute to EC. In figure 1.6(b), $\rho Y_e = 10^8$ g·cm^{-3} therefore only transitions to 1.5 MeV and 2.0 MeV contribute strongly to EC at low temperature since they are below the cut-off set by the Fermi energy. At this ρY_e, only after a sufficient increase in temperature would 2.5 MeV and 3.0 MeV begin to contribute.

Figure 1.7 represents a combination of temperature and density effects. The logarithm of the EC rate is plotted against the logarithm of ρY_e from results of EC rate calculations with artificial input data. These calculations were performed with a constant B(GT)=1, $Q_{g.s.} = 0$ MeV, and excitation energies of 3.0, 6.0, 8.0, and 20.0 MeV, respectively. At low temperature (figure 1.7(a)), the electron gas is degenerate so only captures into states below the Fermi energy set by ρY_e significantly contribute to the rate. Once the density has sufficiently increased, ε_F will increase and EC into states at higher excitation energies can contribute. This can be seen by the sharp increase in EC rates calculated for each excitation energy in figure 1.7(a). Captures into the lowest excitation energy of 3.0 MeV contribute strongly at $\rho Y_e \sim 3$ g·cm^{-3} (solid black line), whereas captures into the highest excitation energy of 20 MeV only contribute at $\rho Y_e \sim 9$ g·cm^{-3} (dot-dashed blue line). At higher temperature, this is complicated since degeneracy has been lifted so captures into higher excitation energies can contribute, even at lower densities. Figure 1.7(b) shows that at a temperature of $T = 10$ GK, the Fermi surface is smeared such that captures to states at all excitation energies can significantly contribute to EC.

1.3.2 Excitation Energy in Daughter Nuclei

As discussed in the previous section, the excitation energy of the daughter state relative to the Fermi energy is a very important factor in the calculation of the EC rate. This is emphasized in figure 1.8. EC rates were calculated for a GT transition with B(GT)= 1 and $Q_{g.s} = 0$ MeV for which the daughter nucleus excitation energies (horizontal axis of Fig. 1.8) were varied from 0.1 to 8.0 MeV. The rates for two densities are plotted against daughter excitation energy at $T = 0.01$ GK. At a density of $\rho Y_e = 10^8$ g·cm^{-3}, figure 1.5 shows that the Fermi energy resides at ~ 2.5 MeV which is indeed where the drop off in rates occurs for the black dotted line in figure 1.8. Figure 1.5 also shows that for $\rho Y_e = 10^9$ g·cm^{-3}, the Fermi energy is ~ 5 MeV and that is location of the sharp decline in EC rates for the solid blue line.

Although the sharp drop in the EC rate at the Fermi energy is not as dramatic at finite temperatures since the Fermi surface is smeared out, it is clear that it is critical that excitation energies are well-predicted by theoretical models for GT transition strengths. For a level near the Fermi surface, even a small shift could result in a large change in the EC rate. This is particularly true if there are no or only very weak transitions to states below the Fermi surface. Likewise, when calculating EC rates from GT strength distributions extracted from experimental data it is important that excitation energy distributions are determined with high resolution and small systematical errors.

1.3.3 Gamow-Teller Transition Strength

It is clear from equation 1.9 that EC rates are proportional to B(GT). This is visualized in figure 1.9. EC rates were calculated for three cases; for all three, the excitation energy
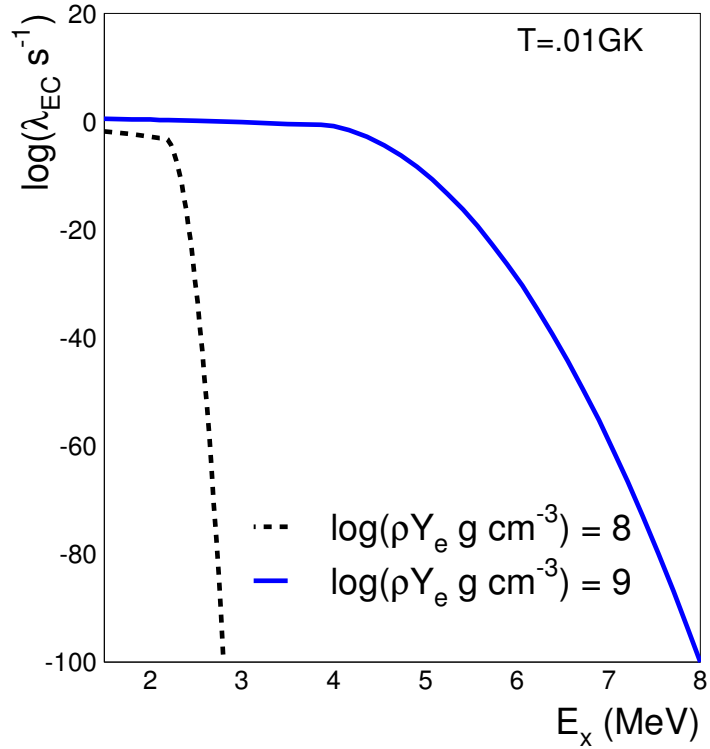
Figure 1.8: Electron-capture rates were calculated for various excitation energies with $Q_{g.s.} = 0$ MeV and constant B(GT)= 1. Two relavant densities were chosen ($\rho Y_e = 10^8$g·cm^{-3} and $\rho Y_e = 10^9$g·cm^{-3}) for $T = 0.01$ GK. The sharp cut-off in the electron-capture rates for the two densities occur at approximately 2.5 and 5.0 MeV respectively, in agreement with figure 1.5.

of the daughter state was set to $E_x = 3$ MeV (with $Q_{g.s} = 0$ MeV) but the B(GT)s were set to 1, 2, and 3, respectively. In the figure, the ratio of B(GT)= 2 and 3 to B(GT)= 1 are plotted. As expected, the ratios are independent of density and are simply equal to the ratios of the corresponding B(GT)s. Therefore, errors introduced in the calculated EC rates are proportional to the uncertainties in the theoretical B(GT) strengths, or the uncertainties in the extraction of B(GT) for the experimentally obtained strengths.

It has been shown that there are four factors that alter the EC rates: ρY_e, temperature, excitation energy, and GT strength. Accurate EC rate calculations are highly dependent on the placement of the excitation energies of the daughter nucleus relative to the Fermi energy for given stellar density. Near the Fermi surface, small shifts in the calculated or experimentally extracted excitation energy can change the rate associated with the capture into that state by large factors. The lower the stellar temperature, the higher the uncertainty will be that is induced by the misplacement of states near the Fermi surface. Therefore, if there are only a few or no states available for weak transitions below the Fermi energy, the total EC rate would be highly dependent on the states located near the Fermi energy. However, if there is a significant amount of strength found below the Fermi energy, the EC rate would mostly be determined by transitions into these states. The uncertainty in the EC rate calculation would then be determined by a combination of both uncertainties due to calculated/experimental B(GT) strengths and the placement of daughter excitation energy states. It is concluded that it is crucial that theory accurately predicts the location of daughter states and to a somewhat lesser extent, the strength associated with captures into those states.
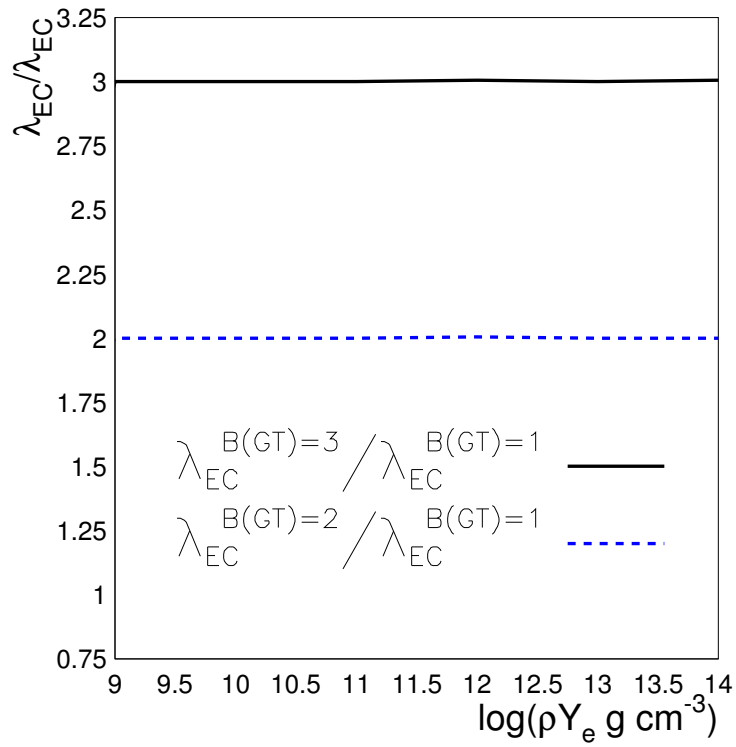
Figure 1.9: Electron-capture rates were calculated for B(GT)= 1, 2, and 3 at $E_x = 3$ MeV and $Q_{g.s} = 0$ MeV. It can be seen that the ratio of the rates is simply the ratio of the Gamow-Teller strengths.

1.4 Outline

The case has been made that theoretical Gamow-Teller transition strengths need to be accurately predicted in order to calculate reliable electron-capture rates. The means by which to test the theory against experiment will be presented. The step-by-step process of calculating electron-capture rates for both theoretical and experimental Gamow-Teller strengths will be described in chapter 2. The procedure to use the shell-model to theoretically predict GT strengths will be described in chapter 3. A comparison study using newly determined Gamow-Teller strengths for the reaction $^{56}\text{Fe}(t,^3\text{He})^{56}\text{Mn}$ and results from a previous $^{56}\text{Fe}(n,p)^{56}\text{Mn}$ experiment along with theory will be investigated in chapter 4. Finally, the thesis is concluded with remarks in regards to the results in chapter 5.

Chapter 2

Electron Capture Rate Calculation

2.1 Overview

The EC rates are calculated using a program based on the method proposed by Fuller, Fowler, and Newman in their 1980 paper [14] mentioned in chapter 1. The program, "nucleus_iterator.f", is written in Fortran by Sanjib S. Gupta in 2006 [21] modified for the use with a continuous chemical potential calculated from an electron-positron equation of state routine [22] instead of the original discrete grid provided by the program. The EC rates are calculated using equation 1.9. There are five input files:

- **"nucleuslist.dat"**: contains Z and A of parents
- **"cap_daughters_ZA"**: contains daughter transition energies and strengths
- **"cap_header_ZA"**: contains information about the reaction
- **"cap_parents_ZA"**: contains parent nucleus information
- **"cap_transitions_ZA"**: contains transition strength information

where Z and A are the three-digit atomic and mass number. All Z and A numbers must be three-digits with zeroes filling in the spaces in front for one and two-digit numbers. For example, if Z=1 and A=2, the extension would be 001002. The output file is named "phaseout_ZA" which contains the EC rates at various temperatures and densities. All input and output files are contained within the subdirectories of the "ecrates_temp" folder.

The "ecrates_temp" folder is located within the "ceclub" portion of the projects folder on intranet (i.e. "/projects/ceclub/ecrates_temp".) When creating an "ecrate" directory for the first time, it is important to copy this directory and change the label "temp" to the user name. This will identify the user of the directory and decipher it from other CE group member's working "ecrate" directories. The files contained within this directory have been prepared to move to a new "ecrates_user" directory without having to adjust how files are called. There four subdirectories with fixed names:

- "codes.dir"
- "expl.dir"
- "input.dir"
- "phaseoutfiles.dir"

The contents of these directories will be discussed in detail in following sections.

2.2   Codes Directory

The "codes.dir" contains the EC rate program "nucleus_iterator.f" along with the referenced programs. These files do not need modified. The "codes.dir" directory also contains "nucleuslist.dat" as seen in figure 2.1, which is used by the program to determine the parent

Figure 2.1: This is the structure of "nucleuslist.dat". It contains the atomic and mass number of the parent nucleus and can be found within the codes directory.

nucleus. The "filecreator" program discussed in section 2.3 modifies this file and it does not need changed by hand. Details on how to run the program "nucleus_iterator.f" are in section 2.6. The program accepts GT strengths and energies, and outputs EC rates and neutrino-loss rates. It uses a standard temperature grid of .01 GK - 100 GK and ρY_e ranges from 10 g·cm^{-3} - 10^{14} g·cm^{-3}. The temperatures can be found in "gmp_temp" if changes are necessary and ρY_e is located within a do-loop in "nucleus_iterator.f". If changes are made to the do-loop, recompiling is necessary and is described in section 2.6.

2.3   Input Directory

As the name implies, "input.dir" contains the input files for the program. These are the four files mentioned in section 2.2 that begin with "cap_". To ease file creation, there exists a program titled "filecreator.f" that creates from one input file the aforementioned files along with the fifth mentioned in section 2.1, "nucleuslist.dat". A sample "inputfile" is located in the input directory and is shown in figure 2.2(a).

The first row contains the relevant information about the mother and daughter nuclei. An explanation of what each value is can be found in figure 2.2(b). The parent excitation energy is always 0.000 MeV since the parent nucleus is in the ground state; furthermore, with one parent state the spin will be 0.0. Z and A are the atomic and mass number of the parent nucleus. The Q-value is the energy difference between the parent ground state

(a) Input File Data

Parent Excitation Energy (MeV)	Parent Spin	Z Parent	A Parent	Q- Value	Number of Daughter States	Number of Parent States	Number of Transitions
Parent State Number	Daughter State Number	Daughter Excitation Energy (MeV)	Gamow- Teller Strength				
⋮	⋮	⋮	⋮				

(b) Input File Definition

Figure 2.2: This is the structure of "inputfile" which creates the five files necessary to run the electron-capture program. a) This is an example of data that was placed in "inputfile". b) This is an explanation of each of the values in "inputfile". It requires mother and daughter nucleus energies and spin, number of mother and daughter states, Q-value of the transition, proton and mass number, and B(GT) values.

Figure 2.3: The parent file contains the excitation energy in MeV and the spin of the parent nucleus.

and the daughter ground state less the rest energy of the electron, calculated with nuclear masses, $Q_{g.s.} = M_m - M_d - m_e$ in MeV. Figure 1.4 gives a schematic of this process. The number of daughter and parent states is the total number of states for each nucleus. If there is one parent state, the number of transitions will equal the number of daughter states.

The second row begins listing the transition information as shown in figure 2.2(b). After running the program, the four "cap_" files located in "input.dir" are created. Eight example "cap_" folders are located in the "ecrates_temp" input directory. Half of those files are experiment and the other half are theory. The differences in theory and experiment will be discussed in chapter 3.

- Parents File

  The "cap_parents_ZA" file contains the information about the initial nucleus. This is where the file creator program places the parent excitation energy and parent spin in one row by two columns as seen in figure 2.3.

- Daughters File

  The file creator program places all daughter excitation energies from the input file into a single column in "cap_daughters_ZA" as shown in figure 2.4.

- Transitions File

  The "cap_transitions_ZA" file contains three columns.

```
0.0180
0.5220
0.9790
1.0430
1.4270
1.5130
1.7590
1.9560
2.1200
2.4190
2.4870
2.6280
2.8020
2.8100
2.8870
2.9320
2.9670
3.0230
```

Figure 2.4: The daughter file contains the excitation energy in MeV of all the daughters states.

- Total number of parent states (usually 1)

- List of daughter states

- $\log(ft)$ for each transition

Figure 2.5 gives an example of what the "cap_transitions_ZA" file looks like. In equation in chapter 1, "ft" are the nuclear matrix elements for a weak reaction. The "filecreator.f" calculates the logarithm of this number and places it in the "cap_transtions_ZA" file.

- Header File

  Finally, the "cap_header_ZA" file shown in figure 2.6 contains one column which is from top down:

  - number of parent states

  - number of daughter states

  - atomic number of parent

  - mass number of parent

```
1    1    6.2669
1    2    7.5457
1    3    6.8467
1    4    7.3696
1    5    5.3769
1    6    6.5914
1    7    6.4488
1    8    7.3696
1    9    6.4665
1   10    6.7006
1   11    4.8681
1   12    7.0016
1   13    5.5939
1   14    5.9491
1   15    5.2704
1   16    4.8280
1   17    5.7294
```

Figure 2.5: The transitions file contains the parent state number, daughter state number, and $\log(ft)$ for each transition.

```
1
277
27
59
-1.5648
277
```

Figure 2.6: The header file contains one column with the number of parent states, number of daughter states, atomic and mass number of the parent nucleus, $Q_{g.s}$, and the number of transitions.

- $Q_{g.s.}$

- number of transitions

2.4   Explanation Directory

The "expl.dir" directory contains information about the electron-capture program. It is not necessary to modify any of the files within this folder. The notes about the program are contained here along with a "readme" file discussing the file structure presented in section 2.3.

26

2.5   Phaseoutfiles Directory

The "phaseoutfiles.dir" directory contains the result of the calculation. The program produces a file labeled "phaseout_ZA" as mentioned in 2.1. It is made up of four columns from left to right:

- $\log_{10}(\rho Y_e \text{ g·cm}^{-3})$
- Temperature (GK)
- $\log_{10}(\lambda_{ec} \text{ s}^{-1})$
- $\log 10(\lambda_\nu \text{ s}^{-1})$

where the first, $\log_{10}(\rho Y_e \text{ g·cm}^{-3})$, is the density of the star. Following are the temperature of the star, the logarithm of the EC rates, and the logarithm of the neutrino energy loss rates. Here, the neutrino energy loss rate is the energy loss associated with the transition from parent state to daughter state in units of MeV s^{-1} [14].

2.6   Running the Program

When the programs are first used, they need to be compiled. Compiling of the file creation programs must be done in the input directory. In this directory, the "gfortran" compiler is to be used with the flag '-o'.

$>$ gfortran filecreator.f -o filecreator

$>$ gfortran filecreator_theory.f -o theory_filecreator

This creates executables named "filecreator" and "theory_filecreator" which will be used to run the file creation programs. The program "filecreator_theory.f" takes into account a

27

quenching factor for GT transitions and must be used to create the file for B(GT) distributions calculated in shell-model theory. This is discussed in chapter 3. When compiling the "nucleus_iterator.f" program it is necessary to include three files total during compilation that are called by the program. The programs, "eos_wrap" and "helm.f" are included with "nucleus_iterator.f" to account for the continuous chemical potential. This creates an executable "ecrates" that when run, will calculate the electron-capture rates. To compile:

> gfortran nucleus_iterator.f eos_wrap.f helm.f -o ecrates

After both programs have been compiled, it is not necessary to compile them again unless changes have been made to the program. An important note is that the program will look for the "cap_" files in the form "cap_header_ZA", etc. If the program is being run for the same nucleus but for both experiment and theory, it is necessary to add an extension *after* the program has run to the old "cap_" files to prevent them from being overwritten. For example, if the EC rates have been calculated for GT strengths obtained from an experiment on ^{45}Sc, the "cap_" files will need an extension before running either file creator program again. An example of how this could be done is to rename "cap_parents_021045" to "cap_parents_021045_exp". For further reference, the "ecrates_temp_input.dir" folder contains example "cap_" folders. The following steps will need to be taken every time the program is run.

1. In the "input.dir" directory, modify the "inputfile".

2. In the "input.dir" directory, run "filecreator" or "theory_filecreator".

3. From the "codes.dir" directory, run "ecrates".

There should now exist a "phaseout_ZA" file in "phaseoutfiles.dir" for this parent nucleus.
A common error that EC rate calculation program will encounter is a run time error when
it reaches a "load_cap_" file. This happens when the "cap_" file already exists for that
nucleus. After adding an extension to the old file, this error will be resolved. The EC rate
calculation program will overwrite "phaseout" files so it is important here as well to add
extensions to run a particular reaction more than once.

2.7 Analyzing the Results

Any type of plotting program can be used to view the results such as Physics Analysis
Workstation (PAW) [23], gnuplot [24], or ROOT [25]. Included in "ecrates_temp" is an
example of analysis using PAW. The PAW website contains tutorials and references that can
be used in combination with the example for a user new to PAW (see Ref. [23]).

PAW files are those with the extension ".kumac". The example located in the folder
is "phasoutgraphs_023050_demo_exp.kumac". Executing a ".kumac" file with PAW will
create either a Post Script file or Encapsulated Post Script file depending on the what was set
by the user within the ".kumac". To execute the ".kumac" from "ecrates_temp\phaseoutfiles":

> PAW

> Workstation type (?=HELP) <CR>=1 : PRESS <ENTER>

PAW > exec phaseoutgraphs_023050_demo_exp

This command will produce a figure such as that shown in figure 2.9. Here, the logarithm
of the EC rate was plotted against temperature for fixed ρY_e. Only a range of ρY_e that are

Figure 2.7: Typing the PAW command brings the user to the welcome screen.

Figure 2.8: After pressing <enter>, this PAW command prompt is shown.

relevant in late stellar evolution are shown [5, 26]. With the EC rate calculation program described, it is now necessary to understand how to get GT strengths to input into the program.
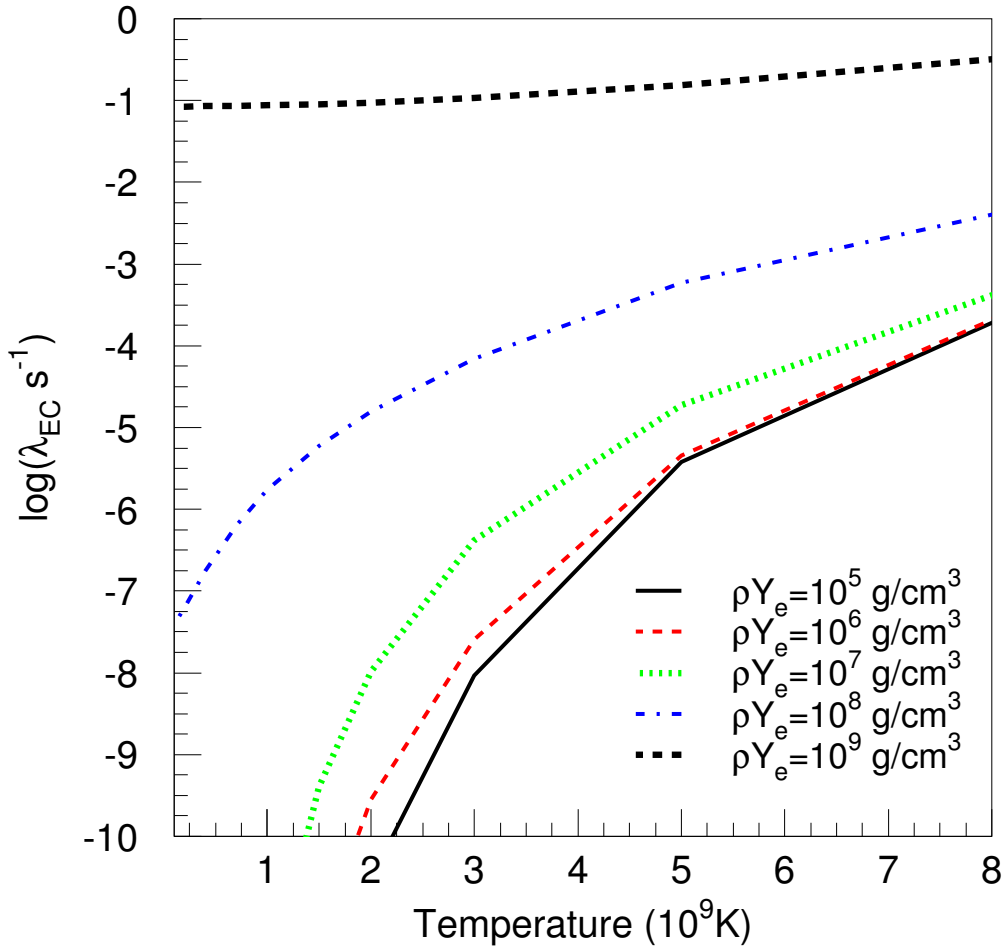
Figure 2.9: This figure is an example of a PAW output for electron-capture on ^{50}Ti. The y-axis is the log of the electron-capture rate and the x-axis is the temperature. The densities are held constant and are represented by each line.

Chapter 3

Obtaining Gamow-Teller Strengths

3.1 Experimental Gamow-Teller Strengths

EC rates are an important input for astrophysical simulations of supernovae as described in chapter 1. A large number of isotopes play a role, including many that are unstable. In addition, due to the relatively high stellar temperatures, excited states can be thermally populated and EC can take place on these states. Therefore, it is impossible to measure all GT strength distributions of relevance for EC in stellar environments and theoretically calculated GT strength distributions must be heavily relied upon. Because stellar evolution models are quite sensitive to the EC rates, it is important that the theoretical rates are benchmarked against experiment. Since GT strengths extracted from $\beta-$decay experiments are only available in a limited $Q-$value window, CE reactions have become the preferred tool to measure the relevant GT strength distributions. The extraction of GT strengths from CE experiments is based on the proportionality between B(GT) and the differential cross section at vanishing linear momentum transfer $\left(\frac{d\sigma}{d\Omega}\big|_{q=0}\right)$ for GT transitions at intermediate

energies [27]:

$$\frac{d\sigma}{d\Omega}\bigg|_{q=0} = \hat{\sigma}_{GT}B(GT). \tag{3.1}$$

The GT unit cross section $\hat{\sigma}_{GT}$ can either be directly calibrated (if the ground-state to ground-state transition has a known B(GT) from a β-decay half-life measurement) or it can be determined from a mass-dependent relationship such as that developed in Ref. [28]. This proportionality is remarkable since the same information on transitions mediated by the weak nuclear force (EC and $\beta-$decay) can be obtained from the CE reaction, which is mediated by the strong nuclear force. In addition to the interest for nuclear astrophysics, GT transition strengths have successfully been determined in CE experiments for a variety of other purposes: nuclear structure, neutrino physics, and giant resonances and their macroscopic properties.

The proportionality of Eq. 3.1 was originally established for nucleon-induced CE (p,n) and (n,p) reactions, but has been shown to also hold for CE experiments with composite probes such as $(d,^2\text{He})$ [29], $(^3\text{He},t)$, and $(t,^3\text{He})$ [18]. For the purpose of extracting GT strengths of relevance for EC in supernovae the (n,p), $(d,^2\text{He})$, and $(t,^3\text{He})$ reactions have been commonly used.

Use of the (n,p) reaction has the advantage that the reaction mechanism is the simplest, but it suffers from relatively poor resolution (~ 1 MeV). With the $(d,^2\text{He})$ reaction, resolutions of 100-200 keV can be achieved, but the reaction mechanism is complex and there are presently no readily available facilities where $(d,^2\text{He})$ experiments can be performed. With the $(t,^3\text{He})$ reaction, resolution of 250-400 keV can be achieved and the reaction mechanism has been well studied using the inverse $(^3\text{He},t)$ reaction [18]. The present experimental situation can be summarized as follows. GT strengths for $pf-$shell nuclei have been extracted

33

from many (n,p) experiments and to a lesser extent from $(d,^2\text{He})$ experiments. $(t,^3\text{He})$ experiments are relatively new and only a few cases have been studied. However, further $(t,^3\text{He})$ experiments are planned. In addition, first efforts to extract GT strengths from rare isotopes for astrophysical purposes have been undertaken. Recently, the GT strength distribution from ^{56}Ni was extracted from a (p,n) experiment in inverse kinematics [30].

To extract the $\Delta L = 0$ GT strength from CE experiments, it must be separated from contributions of excitations associated with higher multi-pole transfers through a multi-pole decomposition analysis (MDA). This method is based on the fact that the $\Delta L = 0$ angular distribution is strongly forward peaked, unlike the distributions associated with $\Delta L > 0$ excitations. After the MDA, the extracted $\Delta L = 0$ cross sections can be extrapolated to $q = 0$ based on the results of a distorted-wave born-approximation (DWBA) [31]. Thereafter, they can be converted to B(GT)s using equation 3.1.

3.2   Theoretical Gamow-Teller Strengths

There are two theoretical methods used in this work to compare calculated Gamow-Teller strengths with experiment:

- by using the shell-model code NuShellX@MSU [32] and

- Quasi-particle Random Phase Approximation (QRPA).

The QRPA calculations were obtained from Ref. [33,34]. NuShellX@MSU calculations were performed in the $pf-$model space using two Hamiltonians: KB3G [35, 36] and GXPF1a [37,38] and will be described in the following section.

Figure 3.1: After double-clicking "login-aaa", to begin NuShellX@MSU, type "shell" in the prompt.

3.2.1 Using NuShellX@MSU

NuShellX@MSU can be obtained from Ref. [32]. Contained within the NuShellX@MSU package is a "help.pdf" file which outlines the procedure for NuShellX@MSU installation. After NuShellX@MSU has been installed, accessing "login.aaa" will allow the user to log into the program. By typing "shell" into the prompt shown in figure 3.1, the program will begin by requesting the name of the batch file to be created. By responding with a batch file name, the user is choosing to answer the questions that follow in a step-by-step manner. However, it is possible to answer the questions beforehand with the creation of an answer file with the extension ".ans". An answer file for the reaction ^{45}Sc$\rightarrow^{45}$Ca is shown in figure 3.2. By responding to the question regarding the batch file name with the name of the answer file, the program will skip to the end of the question section and provide the user with a batch file name. At this point, by typing the name of the batch file into the prompt, the NuShellX@MSU calculation will begin.

3.2.1.1 Components of the Answer File

This process describes the creation of an answer file to calculate Gamow-Teller transition strengths using NuShellX@MSU. The first two sections of the file create the wave functions

```
------------------------------------------------
lpe,   1                       ! option (lpe or lan), neig (zero=10)
fp                             ! model space (*.sp) name (a8)
n                              ! any restrictions (y/n)
gx1a                           ! interaction (*.int) name (a8)
 21                            ! number of protons
 45                            ! number of nucleons
 3.5, 3.5, 0.0,                ! min J, max J, del J
  1                            ! parity (0 for +) (1 for -) (2 for both)
------------------------------------------------
lpe, 100                       ! option (lpe or lan), neig (zero=10)
 20                            ! number of protons
 45                            ! number of nucleons
 2.5, 4.5, 1.0,                ! min J, max J, del J
  1                            ! parity (0 for +) (1 for -) (2 for both)
------------------------------------------------
den                            ! option
t                              ! 1, 2 or t
f51517                         ! initial file name (default = f50519)
  1                            ! max number
f50515                         ! final file name (default = f50519)
 100                           ! max number
 3.5, 3.5, 0.0,                ! min, max J, del J for f51517
 2.5, 2.5, 1.0,                ! min, max J, del J for f51515
n                              ! restrict tensor y/n
------------------------------------------------
den                            ! option
t                              ! 1, 2 or t
f51517                         ! initial file name (default = f50519)
  1                            ! max number
f50517                         ! final file name (default = f50519)
 100                           ! max number
 3.5, 3.5, 0.0,                ! min, max J, del J for f51517
 3.5, 3.5, 1.0,                ! min, max J, del J for f51517
n                              ! restrict tensor y/n
------------------------------------------------
den                            ! option
t                              ! 1, 2 or t
f51517                         ! initial file name (default = f50519)
  1                            ! max number
f50519                         ! final file name (default = f50519)
 100                           ! max number
 3.5, 3.5, 0.0,                ! min, max J, del J for f51517
 4.5, 4.5, 1.0,                ! min, max J, del J for f51519
n                              ! restrict tensor y/n
st                             ! stop
```

Figure 3.2: The series of questions asked by the program can be answered with the creation of an answer file.

for the parent and daughter nuclei. The following sections of the file provide information for calculating the transition amplitudes for the wave functions. The structure of the example answer file shown in figure 3.2 is described.

- **lpe, 1**: The first section is for the parent nucleus information. The term "lpe" notifies NuShellX@MSU to create wave functions. The number is set to one because there is one parent ground state.

- **fp**: The "fp" is the model space name.

- **n**: Generally, there are no restrictions to the model space so this is set to "n" for "no".

- **gx1a**: The interaction Hamiltonian name in this case is "gx1a" which is also referred to outside of the answer file as GXPF1a. For weak-reaction rates, the interaction Hamiltonian KB3G is also used and is labeled "kb3g" in the answer file.

- **21**: Number of protons in the parent nucleus.

- **45**: Total number of nucleons in the parent nucleus.

- **3.5, 3.5, 0.0,**: Minimum and maximum total angular momentum (J) of the wave functions to be generated. The third number is the total angular momentum step size. Since the parent nucleus will be restricted to the ground state, the minimum will equal the maximum and the step will be zero. Ref. [39] can be used to look up the total angular momentum of the ground state.

- **1**: The parity of the parent ground state. For positive parity enter "0", for negative enter "1". The parity can be referenced using Ref. [39].

- **lpe, 100**: NuShellX@MSU is notified that wave functions are to be created for a daughter nucleus. The choice "100" is used to create 100 eigen functions.

- **20**: Number of protons in the daughter nucleus.

- **45**: Number of nuclei in daughter nucleus.

- **2.5, 4.5, 1.0,**: Minimum and maximum total angular momentum of the daughter nucleus that can be probed through a GT transition. The last number is the step size of the total angular momentum. If the total angular momentum of the parent ground state is J_i then the possible values of J_f can be found with the condition that $J_f - 1 \leq J_i \leq J_f + 1$. If $J_i = 0$ then $J_f \neq 0$.

- **1**: Parity of the daughter states. In a GT transition, parity is constant so this will be the same as the ground state of the parent nucleus.

- **den**: This notifies NuShellX@MSU that the overlap will be calculated between two wave functions.

- **t**: This tells NuShellX@MSU to calculate a one-body transition density.

- **f51517**: Initial wave function name. NuShellX@MSU uses a six letter naming scheme: abcdef. a) The fp-model space is "f" in the naming convention. b) When the "f" is followed by either a "5" or "4", the file will refer to "GXPF1a" or "KB3G", respectively. c) Number of valence protons. d) Number of valence nucleons. e) Parity (0 for +, 1 for −). f) Two times the parent total angular momentum ($2J_i$). A more in depth explanation of the naming procedure can be found in the "login.bat" file included with the NuShellX@MSU installation pack.

- **1**: Total number of initial states. There is one parent state, thus this is unity.

- **f50515**: Final wave function name. This is the lowest total angular momentum wave function for the daughter nucleus. The name is determined with the same procedure as above except part f) will be two times the lowest total angular momentum of the daughter nucleus.

- **100**: Number of final states. In this answer file, it is requested that NuShellX@MSU calculate up to 100 states in the daughter nucleus for this total angular momentum value.

- **3.5, 3.5, 0.0,**: Minimum and maximum total angular momentum for parent state.

- **2.5, 2.5, 1.0,**: Minimum and maximum total angular momentum for daughter state with the minimum total angular momentum. The last number is the step size for total angular momentum.

- **n**: No restrictions to the model space.

- **den**: NuShellX@MSU is notified another overlap is to be calculated.

- **t**: Overlap for one-body transition density.

- **f51517**: Initial state name.

- **1**: Initial number of states for the parent nucleus.

- **f50517**: Final state name for next step in total angular momentum.

- **100**: Number of final states for this angular momentum.

- **3.5, 3.5, 0.0,**: Total angular momentum for the parent ground state.

- **3.5, 3.5, 1.0,**: Total angular momentum for the daughter state. The next step in total angular momentum is chosen.

- **n**: No restrictions to the model space.

- **den**: The final density overlap will be calculated.

- **t**: Overlap for one-body transition density.

- **f51517**: Parent ground state wave function name.

- **1**: Initial number of states for the parent nucleus.

- **f50519**: Daughter state wave function name for the highest total angular momentum in the daughter nucleus.

- **100**: Number of final states for this angular momentum.

- **3.5, 3.5, 0.0,**: Total angular momentum for the parent ground state.

- **4.5, 4.5, 1.0,**: Total angular momentum for the daughter state. This is the maximum total angular momentum for the daughter nucleus.

- **n**: No restrictions to the model space.

- **st**: Stop

With the questions answered the program creates a batch file that can be run to calculate the GT transition strengths. Typing the batch file name into the prompt will start the calculation. The computation time can be quite long since the number of "active" nucleons can be large in the pf-shell. Answering "yes" to model space truncations above can allow the user to manually input the number of holes in each shell. This will in effect decrease the computing time however will limit the accuracy of the calculated GT strengths [40].

3.2.1.2 After the Calculation is Complete

The program places the GT strengths in a ".bgt" file. The GT strength information is placed into columns of: energy (MeV), B(GT), and Σ B(GT). The states are grouped by the total angular momentum of the daughter nucleus. Within each group, they are sorted by increasing excitation energy.

If the ground state to ground state transition is a GT transition, the entire daughter excitation energy spectrum has to be shifted down in order to place the lowest excitation energy at 0.0 MeV. If, however, the ground state to ground state transition is not a GT transition,

the lowest lying excitation energy corresponding to a GT transition in the daughter nucleus has to be calculated with NuShellX@MSU. For example, in the reaction ^{46}Ti$\rightarrow^{46}$Sc, the ground state of ^{46}Ti has total angular momentum and parity 0^+. The ground state of ^{46}Sc is 4^+ hence, it is not a GT transition. The first state that can be probed through a GT transition is a 1^+ state at energy 978.2 keV according to the Evaluated Nuclear Structure Data File (ENSDF) [39]. It is possible to use this value to shift the energy levels of ^{46}Sc, however to isolate theory from experiment as much as possible for the purpose of comparison, NuShellX is used to calculate this energy.

An answer file used for this calculation is shown in figure 3.3. It contains a single section for the creation of the wave function for the daughter nucleus. Therefore, the proton number and nucleon number will be that of the daughter nucleus and the total angular momentum range will start from the lowest (0.0 for integer total angular momentum and 0.5 for half integer total angular momentum) to a total angular momentum value that exceeds the maximum probed by the transition. This is to ensure the program will calculate the desired excitation energy state since it needs to include the ground state and the first GT state. After running NuShellX@MSU with the batch file created with this answer file, a level diagram will be constructed. This level diagram will be named with the same heading as the batch file but with the ".eps" extension. The location of the first excited state belonging to a GT transition can be determined from this ".eps" file. The entire GT spectrum will then need to be shifted in order to place the first excited state in the daughter nucleus at this energy.

A quenching factor of 0.74^2 needs to be applied to the GT strengths calculated by NuShellX@MSU in the pf-model space to account for degrees of freedom not included within

```
--------------------------------------------------------
lpe, 2                    ! option (lpe or lan), neig (zero=10)
fp                        ! model space (*.sp) name (a8)
n                         ! any restrictions (y/n)
gx1a                      ! interaction (*.int) name (a8)
 21                       ! number of protons
 46                       ! number of nucleons
 0.0, 6.0, 1.0,           ! min J, max J, del J
 0                        ! parity (0 for +) (1 for -) (2 for both)
st
--------------------------------------------------------
```

Figure 3.3: The answer file used in the generation of the low lying excitation energy spectrum for the daughter nucleus.

the model space [41]. This factor is a constant for nuclei within a major oscillator shell (e.g.

"fp"). With both experimental and theoretical GT strengths secured, EC rates can be cal-

culated and compared.

Chapter 4

Comparisons and Results

With the motivation to compare GT strengths calculated with theoretical models with those extracted from experiments in order to better constrain inputs for astrophysical models, a study has been completed based on the GT transition strengths from ^{56}Fe to ^{56}Mn. ^{56}Fe is located in the $pf-$shell and is a member of a group of nuclei that plays a significant role in core-collapse and thermonuclear supernovae. Select nuclei in this region with half-lives greater than 10^3 s are shown in figure 4.1. By investigating ^{56}Fe, one can thus gain further insight into the ability of theoretical models to predict GT strength distributions used for calculating weak reaction rates of relevance for stellar evolution.

Two experimental probes have been used to extract the GT strengths for the transition of ^{56}Fe to ^{56}Mn: the $(t,^3\text{He})$ and (n,p) reactions. The ^{56}Fe$(t,^3\text{He})$ experiment was completed at Michigan State University's National Superconducting Cyclotron Laboratory with a beam energy of 115 MeV/u [42,43]. The resolution achieved was 400 keV. It is important to note that the results of this experiment are preliminary. The ^{56}Fe(n,p) experiment took place at TRIUMF with a beam energy of 198 MeV [44]. The resolution achieved was 1.3 MeV. A
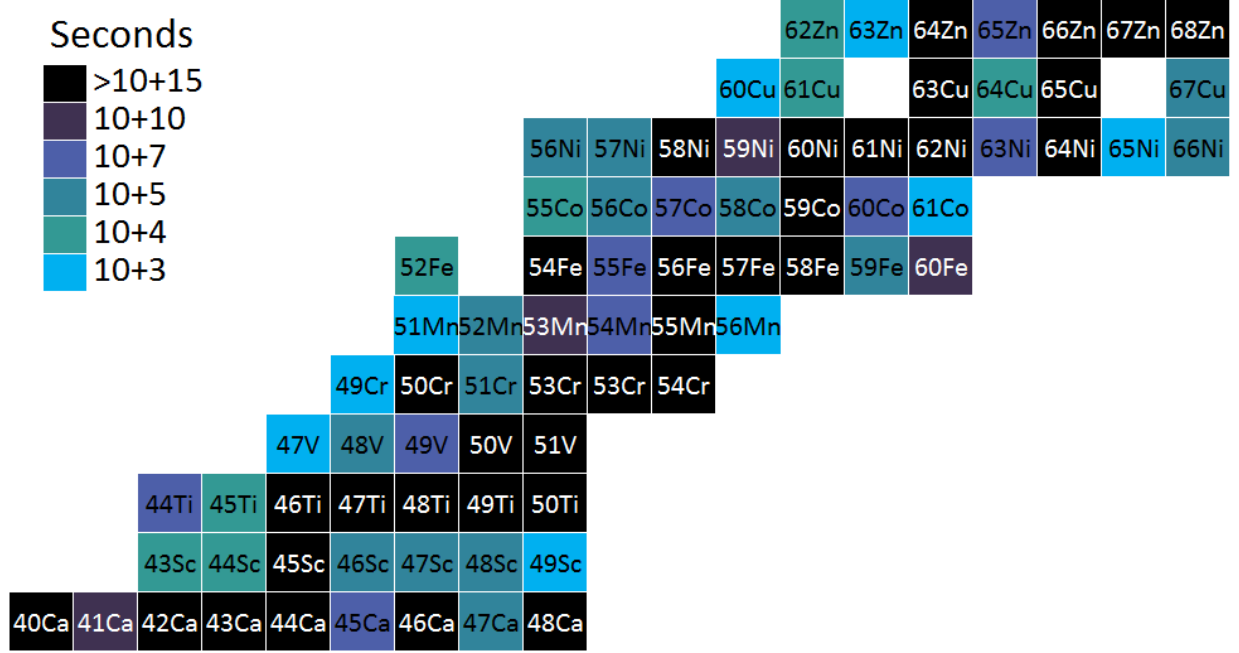
Figure 4.1: Select nuclei in the pf-shell near the valley of stability including ^{56}Fe are shown. The colors represent the half-life of the nucleus.

second experiment has been completed with the ^{56}Fe(n,p) probe, however, the resolution was 2.8 MeV [45]. Therefore, the data from Ref. [44] was chosen for this work simply due to the better resolution. The shell model calculations were performed in accordance with the procedure outlined in chapter 3 using NuShellX@MSU. The QRPA calculations were calculated by Sanjib Gupta. Each GT strength distribution will be discussed as well as the resulting EC rates.

4.1   The Gamow-Teller Strengths

The GT transition strengths used in this work are shown in figure 4.3. Figures 4.3(a-e) show GT strength distributions as a function of excitation energy for the ^{56}Fe(n,p), the ^{56}Fe$(t,^3$He$)$ experiments and the QRPA, KB3G, and GXPF1a, theoretical calculations. Figure 4.3(f) shows the running sums (with excitation energy (MeV)) of the GT strength

Figure 4.2: The ground state and low-lying 1^+ states of ^{56}Mn.

distributions shown in Fig. 4.3(a-e).

$$(a) \ ^{56}\text{Fe}(n,p)$$

Following Ref. [44] the GT strengths are given in 1-MeV wide bins. For the purpose of the EC rate calculation, the entire GT strength in each bin was placed at the central excitation energy of the bin. The data obtained from Ref. [44] contained GT strength (B(GT)=0.136) below $E_x = 0.0$ MeV. For this work, this GT strength was added to the GT strength in the first bin ($E_x = 0.0$ MeV).

$$(b) \ ^{56}\text{Fe}(t,^3\text{He})$$

With the better resolution of 400 keV, two distinct low-lying transitions to 1^+ states could be observed in the ^{56}Fe$(t,^3$He) experiment. By comparing the location of these states to those known from other experiments, they were identified as the 1^+ states at $E_x = .1105$ MeV and $E_x = 1.1677$ MeV, respectively [39]. These two states are shown in the level diagram in figure 4.2. The GT strength at higher excitation energies, extracted using an MDA, were placed into 250 keV-wide bins.

(c) Theory : QRPA

Following the recommendation by the authors, the GT strengths calculated using QRPA do not have a quenching factor applied [34]. To maintain the same vertical scale as the other figures, the GT strengths have been multiplied by a factor of 1/3 in the figure. The lowest 1^+ state found in the QRPA calculation resides at $E_x = 2.52$ MeV. The summed strength is also ~ 2 times larger than that predicted by the shell-model calculations and found by experiment.

(d) and (e) Theory : KB3G and GXPF1a

The GT strengths were calculated using the shell-model in the full fp-model space without truncations. The interaction Hamiltonians KB3G and GXPF1a were used. Both GT strength distributions have been quenched by a factor of $.74^2$ as mentioned in chapter 3. Since the ground state of ^{56}Mn cannot be populated by a GT transition, the low-lying portion of the excitation energy spectrum was calculated for each Hamiltonian, to ensure that the first 1^+ state is located at the appropriate excitation energy relative to the 3^+ ground state discussed in section 3.2.1.2. The GT transition strength calculated with the KB3G interaction (Fig. 4.3(d)) produces stronger first and second excited states than that calculated with the GXPF1a interaction (Fig. 4.3(e)), although the total summed strength is about the same for both shell-model calculations.

(e) Running Sums and Comparisons

A running sum of GT transition strength has been plotted for each GT distribution over the excitation energy range from 2 MeV to 10 MeV. The two experimental results are shown in red with the solid line representing the ^{56}Fe(n,p) and the dotted line representing the ^{56}Fe$(t,^3$He$)$. The two experimental strength distributions appear quite different but that is largely due to the differences in energy resolution since the summed strengths up to 10 MeV are nearly identical. The results from the theoretical calculations are shown in green dashed (QRPA), dotted (KB3G), and dot-dashed (GXPF1a). The summed strength up to 10 MeV for both shell-model calculations is less than that observed experimentally by about 20%. This could partially be due to the fact that some of the quenched GT strength at low-excitation energy has moved to intermediate-excitation energies (5-10 MeV). The QRPA calculations over predict the total amount of GT strength observed experimentally by a factor of 2.

The shell-model calculations performed with the GXPF1a interaction match the high resolution ^{56}Fe$(t,^3$He$)$ data well; the locations and summed strength of the first two transitions are nearly identical (for GXPF1a: $E_{x1} = 0.1300$ MeV and $E_{x2} = 1.2110$ MeV, for ^{56}Fe$(t,^3$He$)$: $E_{x1} = 0.1105$ MeV and $E_{x2} = 1.100$ MeV). The shell-model calculation with the KB3G interaction does slightly poorer; the two low-lying states are too strong and shifted upward by about 400 keV ($E_{x1} = 0.5450$ MeV and $E_{x2} = 1.4640$ MeV). Both sets of shell-model calculations predict strength up to about 6 MeV. The QRPA calculations reproduce the data very poorly; the total strength is too high and the first excited state is placed at an excitation energy about 2 MeV too high ($E_x = 2.5200$ MeV). The reliability of each theoretical GT strength distribution for the purpose of predicting EC rates will be tested in the next section.
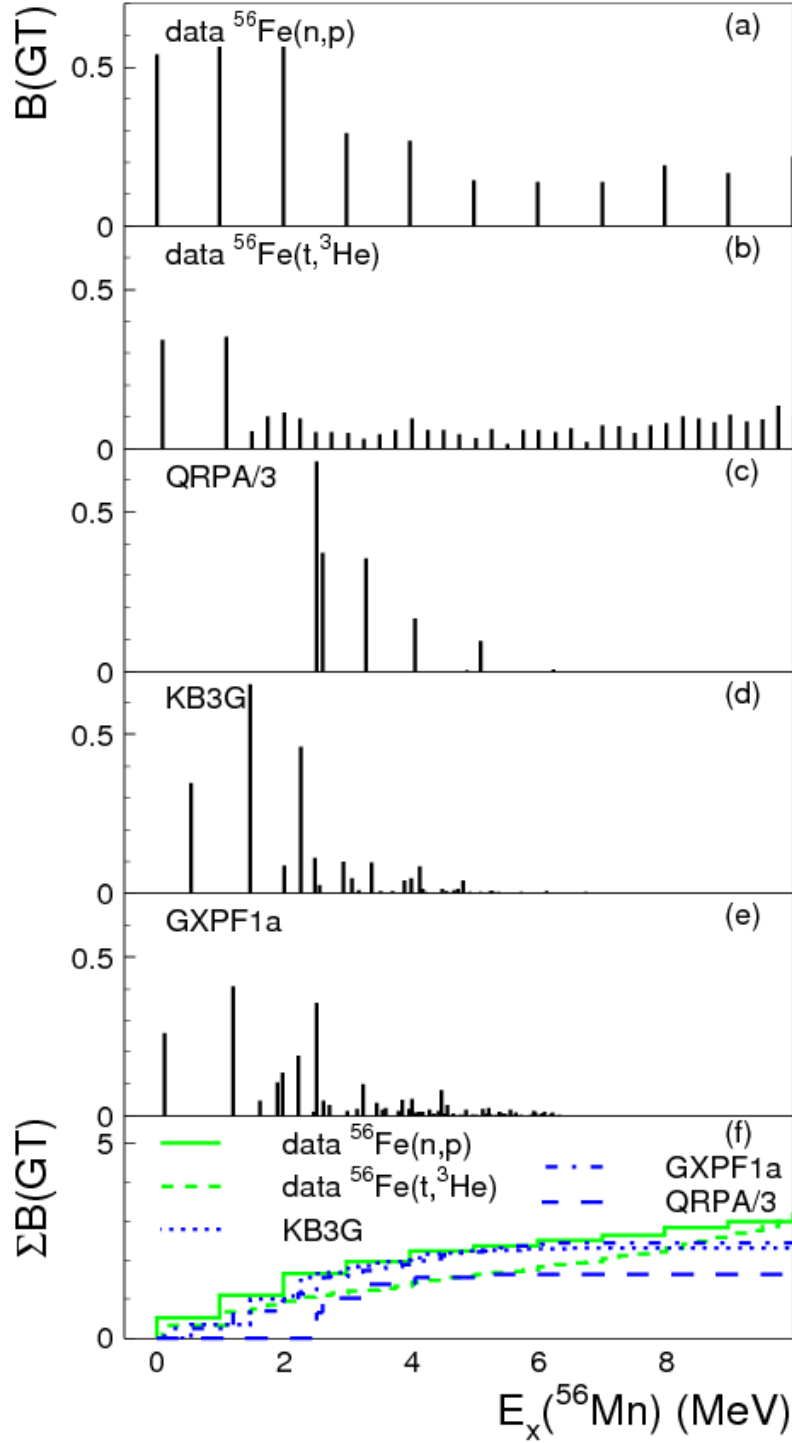
Figure 4.3: GT transition strengths for $^{56}\text{Fe} \rightarrow {}^{56}\text{Mn}$ for (a) $^{56}\text{Fe}(n,p)$ data, (b) $^{56}\text{Fe}(t,^{3}\text{He})$ data, (c) a QRPA calculation (scaled by 1/3), (d) a shell-model calculation using the KB3G interaction Hamiltonian, (e) a shell-model calculation using the GXPF1a interaction Hamiltonian, and (f) a running sum of B(GT) strengths against daughter excitation energy for each of the above cases.

4.2 The Electron-Capture Rate Calculations

EC rates were calculated with each of the GT strength distributions in Fig. 4.3 for the weak reaction $^{56}\mathrm{Fe}(e^-, \nu_e)^{56}\mathrm{Mn}$ using the procedure outlined in chapter 2. The EC rates of relevance for late stellar evolution have been represented in figure 4.4 [26]. Figure 4.4(a) is the result of the EC rate calculations for $\rho Y_e = 10^7$ g·cm^{-3} and figure 4.4(b) is for $\rho Y_e = 10^9$ g·cm^{-3}. Shown in solid and dashed red lines are the logarithm of the EC rate calculations based on the $^{56}\mathrm{Fe}(n,p)$ and $^{56}\mathrm{Fe}(t,^3\mathrm{He})$ data, respectively. Shown in solid, dashed, and dot-dashed green lines are the logarithms of the EC rates calculated based on the QRPA and shell-model calculations using the GXPF1a and KB3G interactions, respectively. The four factors affecting EC rate calculations described in chapter 1 are evident in the calculations performed using the GT strength distributions of figure 4.3.

$$(a)\ \rho Y_e = 10^7\ \mathrm{g \cdot cm^{-3}}$$

At $\rho Y_e = 10^7$ g·cm^{-3}, the Fermi energy is approximately located at 1.223 MeV (see Eq. 1.5). Since $\varepsilon_F \ngtr Q_R = E_x - Q_{g.s} = 4.2072$ MeV, EC can only take place because the degeneracy is lifted at $T \sim 10^9$ K. As discussed in chapter 1 the EC rate in this situation will strongly depend on the location of the lowest-lying daughter states relative to the Fermi level.

Since, due to the poor resolution, some strength extracted from the (n,p) data appears at very low excitation energy, the EC rate is relatively strong (overproduced by a factor of 32) compared to the EC rates calculated from the high resolution $^{56}\mathrm{Fe}(t,^3\mathrm{He})$ data. The EC rate based on the QRPA calculation is much too low (under produced by a factor of 100) because the first daughter state appears at much higher excitation energy. The EC rate

based on the shell-model calculations match that based on the ^{56}Fe($t,^3$He) data quite well. The EC rate based on the KB3G calculations are slightly lower, although the first daughter states are stronger than those seen in the data and in the calculation with the GXPF1a interaction. The reason is that the daughter states appear at higher excitation energies and as discussed in chapter 1, the rates are more sensitive to the location than the magnitude of the strengths. As the temperature is increased, the degeneracy is lifted more and EC rates increasingly occur to higher lying states. As a result, the EC rates converge at high temperature ($T \sim 10^{10}$ K).

$$(b) \ \rho Y_e = 10^9 \ \text{g} \cdot \text{cm}^{-3}$$

The Fermi energy for $\rho Y_e = 10^9$ g·cm^{-3} is 4.67 MeV. Since $\varepsilon_F > Q_R = E_x - Q_{g.s.}$ (with $Q_{g.s} = -4.2027$ MeV) for the first excited states in both sets of experimental data and the shell-model calculations with GXPF1a, the rate is strongly dominated by EC into that daughter state and thus, the differences between the calculated rates are relatively small. Although the first daughter state of the calculation with the KB3G interaction is just above the Fermi energy, it is close enough to have a relatively strong EC rate due to the smearing of the Fermi level at temperatures $\sim 10^9$ K.

At low temperature, the EC rates calculated using the results from QRPA are dramatically under produced by a factor of ~ 3000. The location of the first excited state in the GT strength distribution obtained from the QRPA calculation results in a reaction $Q-$value that is much greater than the Fermi energy ($Q_R = 6.7272$ MeV) so temperature smearing effects have a large impact on the EC rates. The rate of EC is increased by ~ 5 orders of magnitude as temperature increases from $T = 2$ GK to $T = 10$ GK. Note that the total rates are almost 7 orders of magnitude higher than those at the lower densities. At higher
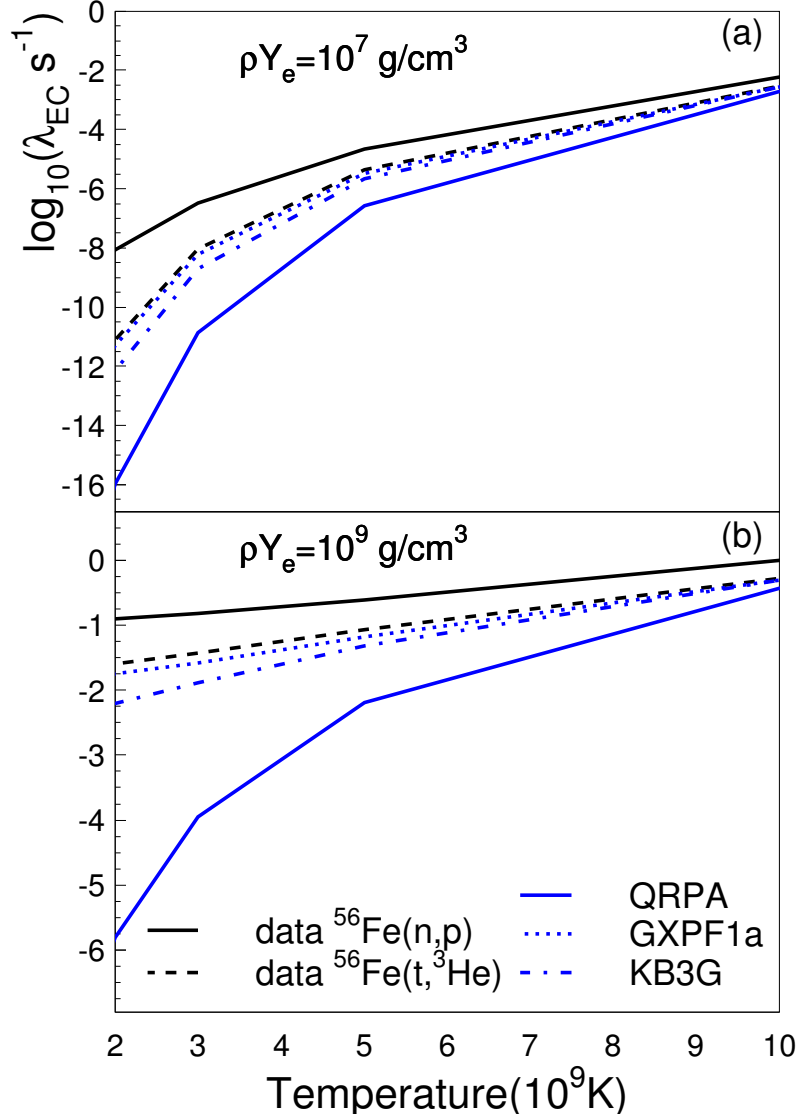
Figure 4.4: Electron-capture rate calculations performed for $^{56}\mathrm{Fe}(e^-,\nu_e)^{56}\mathrm{Mn}$ with experimental and theoretical data plotted against core temperature. (a) EC rates for $\rho Y_e = 10^7 \mathrm{g/cm}^3$ and (b) EC rates for $\rho Y_e = 10^9 \mathrm{g/cm}^3$.

temperatures, the Fermi surface smears out more and the rates slowly increase further, and

converge.

It is concluded that the shell-model calculations with the GXPF1a interaction best match

the high-resolution $^{56}\mathrm{Fe}(t,^3\mathrm{He})$ data, and consequently provide the best estimates when

calculating EC rates. Since the EC rates based on the KB family of interactions (including

KB3G) form the basis for the standard weak-reaction rates library used in many astrophysical calculations [46], it is clear that further improvements to that set of rates can still be made. This result is very similar to that made based on the results from the recent ^{56}Ni(p, n) experiment [30]. Finally, since the QRPA calculations clearly fail in producing accurate EC rates, it is not advised to use these strength distributions in astrophysical calculations where accuracy is essential if other theoretical techniques are available.

Chapter 5

Conclusion

Since weak reactions play a crucial role in the dynamics of core-collapse supernovae and the production of iron group nuclei through thermonuclear supernovae, accurately predicting these rates has great implications in understanding these stellar processes and the production mechanism of a vast number of nuclei in the universe. Calculating EC rates requires GT strengths acquired through both theoretical calculations and experiments. Due to the impossibility to experimentally probe all nuclei relevant in supernova models, theoretically obtained GT strengths have been heavily relied upon, most recently the family of KB interactions in the shell-model. It was shown that EC rates are highly sensitive to results of the GT strength calculations, therefore, it is crucial to constrain these theoretical calculations in order to confidently calculate EC rates. A method used to compare theoretical and experimental GT distributions and the EC rates calculated with those distributions has been presented in this thesis.

In chapter 1, it was shown that there are four factors that affect EC rate calculations: stellar temperature, stellar density (ρY_e), the excitation energy of the daughter nucleus in

a weak reaction, and GT transition strengths. Temperature, ρY_e, and excitation energy were shown to have the strongest influence since they affect rates exponentially whereas the magnitude of the GT transition strengths only affect the rates linearly. The placement of the low-lying states in the daughter nucleus relative to the Fermi energy are the dominate factor, especially at low temperatures. Small shifts in excitation energy can alter the EC rates by orders of magnitude in that case. Since the Fermi energy relies on the density of the core, ρY_e is also a critical parameter. The temperature affects the level of degeneracy; at higher temperatures, states at higher excitation energies in the daughter nucleus become available for EC even if located above the Fermi energy.

In order to better understand these factors and test the accuracy of predicted GT strength distributions, a study of transitions from ^{56}Fe to ^{56}Mn was performed. The choice of this reaction was due, in part, to the important role EC plays on medium-heavy nuclei in late stellar evolution. The GT strength distributions were obtained from two experimental sources: ^{56}Fe(n,p) data and ^{56}Fe$(t,^3$He) data. The experimental results were compared with three sets of theoretical results: QRPA calculations and shell-model calculations using the KB3G and GXPF1a interactions. Comparisons are discussed in chapter 4 and the results show a good agreement between the calculations with the GXPF1a interaction and the high resolution ^{56}Fe$(t,^3$He) experimental data. It was shown that this was largely due to the close proximity of the first excited states in both GT distributions. Conversely, the results of the QRPA calculation had the least agreement since the excitation energy of the first excited state that can be populated is located ~ 2 MeV higher than the first excited state found in any other GT spectrum.

EC rate calculations were then performed on each of these GT distributions. With the

first excited states of the GT distributions using the GXPF1a interaction and ^{56}Fe$(t,^3$He$)$ data appearing in such close proximity in the GT spectrum, the EC rates are similarly close in proximity. The energy differences in the GT distributions in both the ^{56}Fe(n,p) data and those calculated with QRPA were exacerbated in the results of the EC rate calculation. This further demonstrates the importance of an accurate location for the first excited state in the daughter nucleus. It was also confirmed that once the Fermi energy exceeds the first excited state, the influence that temperature has on an EC rate calculation is reduced. This was observed in the EC rate calculations for $\rho Y_e = 10^9$ g·cm^{-3} in which the first excited state for the GT strengths calculated with the GXPF1a interaction and obtained through both the ^{56}Fe $(t,^3$He$)$ and ^{56}Fe(n,p) experiments were below the Fermi energy. Thus, the temperature was seen to have little effect on the calculated EC rates. The GT strengths calculated with the KB3G interaction show still a slight EC rate increase as temperature in increased since the first excited state was only slightly above the Fermi energy. However, the strengths calculated with QRPA still varied significantly with temperature increase. Whereas, the EC rate calculations for $\rho Y_e = 10^7$ g·cm^{-3} in which the first excited state for all GT distributions was above the Fermi energy all increased substantially as temperature was increased.

It is concluded that the shell-model GXPF1a interaction does remarkably well in predicting the GT strength distribution for the reaction ^{56}Fe$\rightarrow^{56}$Mn. As stated before, most astrophysical models have relied on the KB family of interactions. The results of this study show that further improvements can still be made to the current inputs for these models since, in this case, GXPF1a predicts a more accurate GT strength distribution. It is further concluded that for this reaction, the GT strengths predicted by QRPA failed to model the high resolution data. A broader study involving many other nuclei in the pf-shell is

ongoing. If these QRPA calculations are inaccurate for many other cases as they were for ^{56}Fe, it is better to refrain from using weak rates based on this set of QRPA calculations for astrophysical purposes. Finally, high resolution data are the preferred tool for testing weak reaction calculations, where available. However, low resolution data is still a useful tool in constraining theoretical calculations of GT strength distributions.

One of the main aims of this work was to streamline the processes used for analyzing and comparing the strength distributions and EC rates from CE experiments and theoretical models. A number of tools were developed for that purpose and these are currently used to perform a broader study, focusing on all nuclei in the $pf-$shell for which strengths from CE data are available. With the advent of experimental techniques to probe GT strength distributions in rare isotopes (see Ref. [30]), and the construction of next generation rare isotope beams such as the Facility for Rare Isotope Beams (FRIB), there is a realistic opportunity to constrain weak reaction rates to the level required for modern astrophysical simulations. The procedures defined in this thesis will be helpful in assessing the quality of existing and future theoretical calculations based on these forthcoming experiments.

BIBLIOGRAPHY

BIBLIOGRAPHY

[1] Dale A. Ostlie and Bradley W. Carroll. *An Introduction to Modern Steller Astrophysics.* Addison-Wesley Publishing Company, Reading MA, 1996.

[2] F. Richard Stephenson and David A. Green. *Historical Supernovae and their Remnants.* Clarendon Press, Oxford, 2002.

[3] Laurence A. Marschall. *The Supernova Story.* Plenum Press, New York, 1988.

[4] W. Baade and F. Zwicky. On super-novae. *Proc. N. A. S.*, **20**:254–259, 1934. http://www.ncbi.nlm.nih.gov/pmc/articles/PMC1076395/pdf/pnas01745-0006.pdf.

[5] W. R. Hix, O. E. B. Messer, A. Mezzacappa, M. Liebendörfer, J. Sampaio, K. Langanke, D. J. Dean, and G. Martínez-Pinedo. Consequences of nuclear electron capture in core collapse supernovae. *Phys. Rev. Lett.*, **91**:201102, 2003. http://prl.aps.org/abstract/PRL/v91/i20/e201102.

[6] A. Heger, S. E. Woosley, G. Martínez-Pinedo, and K. Langanke. Presupernova Evolution with Improved Rates for Weak Interactions. *The Astrophysical Journal*, **560**:307–325, 2001. http://iopscience.iop.org/0004-637X/560/1/307/.

[7] NASA's Hubble Space Telescope, 2007. http://hubblesite.org/newscenter/archive/releases/2007/10/image/a/.

[8] K. Langanke and G. Martínez-Pinedo. Nuclear weak-interaction processes in stars. *Rev. Mod. Phys.*, **75**:819–862, 2003. http://rmp.aps.org/pdf/RMP/v75/i3/p819_1.

[9] S. E. Woosley and Thomas A. Weaver. The Physics of Supernova Explosions. *ARAA*, 24:205–253, 1986. http://www.annualreviews.org/doi/abs/10.1146/annurev.aa.24.090186.001225.

[10] Koichi Iwamoto, Franziska Brachwitz, Ken′ichi Nomoto, Nobuhiro Kishimoto, Hideyuki Umeda, W. Raphael Hix, and Friedrich-Karl Thielemann. Nucleosynthesis in Chandrasekhar mass models for Type Ia supernovae and constraints on progenitor systems and burning-front propagation. *The Astrophysical Journal Supplement Series*, **125**:439–462, 1999. http://iopscience.iop.org/0067-0049/125/2/439/.

[11] Courtesy NASA/JPL-Caltech, 2008. http://www.spitzer.caltech.edu/images/2060-sig08-016-Vivid-View-of-Tycho-s-Supernova-Remnant.

[12] Franz Osterfeld. Nuclear spin and isospin excitations. *Rev. Mod. Phys.*, **64**:491–557, 1992. http://dx.doi.org/doi:10.1103/RevModPhys.64.491.

[13] H. A. Bethe, G. E. Brown, J. Applegate, and J. M. Lattimer. Equation of State in the Gravitational Collapse of Stars. *Nucl. Phys. A*, **324**:487–533, 1979. http://www.sciencedirect.com/science/article/pii/0375947479905967.

[14] George M. Fuller, William A. Fowler, and Michael J. Newman. Stellar weak-interaction rates for sd-shell nuclei. I - Nuclear matrix element systematics with application to ^{26}Al and selected nuclei of importance to the supernova problem. *The Astrophysical Journal Supplement Series*, **42**:447–473, 1980. http://adsabs.harvard.edu/abs/1980ApJS..42..447F.

[15] G. M. Fuller, W. A. Fowler, and M. J. Newman. Stellar weak-interaction rates for intermediate mass nuclei. II - A = 21 to A = 60. *The Astrophysical Journal*, **252**:715–740, 1982. http://adsabs.harvard.edu/abs/1982ApJ...252..715F.

[16] G. M. Fuller, W. A. Fowler, and M. J. Newman. Stellar weak-interaction rates for intermediate mass nuclei III - Rate tables for the free nucleons and nuclei with A = 21 to A = 60. *The Astrophysical Journal Supplement Series*, **48**:279–319, 1982. http://adsabs.harvard.edu/abs/1982ApJS...48..279F.

[17] G. M. Fuller, W. A. Fowler, and M. J. Newman. Stellar weak-interaction rates for intermediate mass nuclei IV - Interpolation procedures for rapidly varying lepton capture rates using effective log(ft)-values. *The Astrophysical Journal*, **293**:1–16, 1985. http://adsabs.harvard.edu/abs/1985ApJ...293....1F.

[18] G. Perdikakis, R.G.T. Zegers, Sam M. Austin, D. Bazin, C. Caesar, J.M. Deaven, A. Gade, D. Galaviz, C.J. Guess, C. Herlitzius, G.W. Hitt, M.E. Howard, R. Meharchand, S. Noji, H. Sakai, Y. Shimbara, E.E. Smith, and C. Tur. Gamow-Teller Unit Cross-Sections for $(t, {}^{3}\text{He})$ and $({}^{3}\text{He}, t)$ Reactions. *Phys. Rev. C*, **83**:054614, 2011. http://prc.aps.org/pdf/PRC/v83/i5/e054614.

[19] Kenneth S. Krane. *Introductory Nuclear Physics*. John Wiley & Sons, 1988.

[20] R. G. T. Zegers, 2011. Private communication.

[21] Ana D. Becerril Reyes, Sanjib Gupta, Hendrik Schatz, Karl-Ludwig Kratz, and Peter Möller. Electron Capture Rates for Neutron Star Crusts. In *International Symposium on Nuclear Astrophysics - Nuclei in the Cosmos - IX*, 2006. http://pos.sissa.it/ /archive/conferences/028/075/NIC-IX_075.pdf.

[22] F. X. Timmes and F. D. Swesty. The accuracy, consistency, and speed of an electron-positron equation of state based on the onterpolation of the helmholtz free energy. *The Astrophysical Journal Supplement Series*, **126**:126–501, 2000. http://iopscience. iop.org/0067-0049/126/2/501/.

[23] PAW version 2.14/04, 2004. http://paw.web.cern.ch/paw.

[24] gnuplot version 4.4.3. http://www.gnuplot.info/.

[25] ROOT version 5.30/03. http://root.cern.ch/drupal/.

[26] G. W. Hitt, R. G. T. Zegers, Sam M. Austin, D. Bazin, A. Gade, D. Galaviz, C. J. Guess, M. Horoi, M. E. Howard, W. D. M. Rae, Y. Shimbara, E. E. Smith, and C. Tur. Gamow-Teller transitions to ^{64}Cu measured with the ^{64}Zn$(t,^3$He) reaction. *Phys. Rev. C*, **80**:014313, 2009. http://prc.aps.org/pdf/PRC/v80/i1/e014313.

[27] T.N. Taddeucci, C.A. Goulding, T.A. Carey, R.C. Byrd, C.D. Goodman, C. Gaarde, J. Larsen, D. Horen, J. Rapaport, and E. Sugarbaker. The (p,n) reaction as a probe of beta decay strength. *Nucl. Phys. A*, **469**:125–172, 1987. http://dx.doi.org/doi: 10.1016/0375-9474(87)90089-3.

[28] R. G. T. Zegers, T. Adachi, H. Akimune, Sam. M. Austin, A. M. van den Berg, B. A. Brown, Y. Fujita, M. Fujiwara, S. Galès, C. J. Guess, M. N. Harakeh, H. Hashimoto, K. Hatanaka, R. Hayami, G. W. Hitt, M. E. Howard, M. Itoh, T. Kawabata, K. Kawase, M. Kinoshita, M. Matsubara, K. Nakanishi, S. Nakayama, S. Okumura, T. Ohta, Y. Sakemi, Y. Shimbara, Y. Shimizu, C. Scholl, C. Simenel, Y. Tameshige, A. Tamii, M. Uchida, T. Yamagata, and M. Yosoi. Extraction of Weak Transition Strenghts via the (^{3}He,t) Reaction at 420 MeV. *Phys. Rev. Lett.*, **99**:202501–1–4, 2007. http: //prl.aps.org/pdf/PRL/v99/i20/e202501.

[29] H. M. Xu, G. K. Ajupova, A. C. Betker, C. A. Gagliardi, B. Kokenge, Y. W. Lui, and A. F. Zaruba. $(d,^2\mathrm{He})$ reactions at $E_d = 125.2$ MeV. *Phys. Rev. C*, **52**:1161–1165, 1995. http://prc.aps.org/pdf/PRC/v52/i3/pR1161_1.

[30] M. Sasano, G. Perdikakis, R. G. T. Zegers, Sam M. Austin, D. Bazin, B. A. Brown, C. Caesar, A. L. Cole, J. M. Deaven, N. Ferrante, C. J. Guess, G. W. Hitt, R. Meharchand, F. Montes, J. Palardy, A. Prinke, L. A. Riley, H. Sakai, M. Scott, A. Stolz, L. Valdez, and K. Yako. Gamow-Teller Transition Strengths from $^{56}\mathrm{Ni}$. *Phys. Rev. Lett.*, **107**:202501, 2011. http://prl.aps.org/pdf/PRL/v107/i20/e202501.

[31] George Wesley Hitt. *The $^{64}Zn(t,^3He)$ charge-exchange reaction at 115 MeV per nucleon and application to ^{64}Zn stellar electron-capture.* PhD thesis, Michigan State University, 2009.

[32] B. A. Brown and W. D. M. Rae, 2011. http://www.nscl.msu.edu/~brown/resources/resources.html.

[33] Sanjib S. Gupta, 2010. Private communication.

[34] Peter Möller and Jørgen Randrup. New developments in the calculation of β-strength functions. *Nucl. Phys. A*, **514**:1–48, 1990. http://www.sciencedirect.com/science/article/pii/037594749090330O.

[35] E. Caurier, F. Nowacki, A. Poves, and J. Retamosa. Shell model study of the neutrinoless double beta decays. *Nucl. Phys. A*, **654**:973c–976c, 1999. http://www.sciencedirect.com/science/article/pii/S0375947400885838.

[36] A. Poves, J. Sánchez-Solano, E. Caurier, and F. Nowacki. Shell model study of the isobaric chains A = 50. *Nucl. Phys. A*, **694**:157–198, 2001. http://www.sciencedirect.com/science/article/pii/S0375947401009678.

[37] M. Honma, T. Otsuka, B. A. Brown, and T. Mizusaki. New effective interaction for pf-shell nuclei and its implications for the stability of the $N = Z = 28$ closed core. *Phys. Rev. C*, **69**:034335, 2004. http://prc.aps.org/abstract/PRC/v69/i3/e034335.

[38] M. Honma, T. Otsuka, T. Mizusaki, M. Hjorth-Jensen, and B. A. Brown. Effective interaction for nuclei of A = 50-100 and Gamow-Teller properties. **20**:7–12, 2005. http://iopscience.iop.org/1742-6596/20/1/002/.

[39] Brookhaven National Laboratory Jag Tuli, NNDC, 2011. http://www.nndc.bnl.gov/ensdf/.

[40] B. A. Brown and B. H. Wildenthal. Status of the Nuclear Shell Model. *Annu. Rev. Nucl. Part. Sci.*, **38**:29–66, 1988. http://www.annualreviews.org/doi/abs/10.1146/annurev.ns.38.120188.000333.

[41] G. Martínez-Pinedo, A. Poves, E. Caurier, and A. P. Zuker. Effective g_A in the pf-shell. *Phys. Rev. C*, **53**:R2602–R2605, 1996. http://prc.aps.org/abstract/PRC/v53/i6/pR2602_1.

[42] Y. Shimbara, 2011. Private communication.

[43] M. Scott, 2011. Private communication.

[44] S. El-Kateb, K. P. Jackson, W. P. Alford, R. Abegg, R. E. Azuma, B. A. Brown, A. Celler, D. Frekers, O. Häusser, R. Helmer, R. S. Henderson, K. H. Kicks, R. Jeppesen, J. D. King, K. Raywood, G. G. Shute, B. M. Spicer, A. Trudel, M. Vetterli, and S. Yen. Spin-isospin strength distributions for fp shell nuclei: Results for the ^{55}Mn(n,p), ^{56}Fe(n,p), and ^{58}Ni(n,p) reactions at 198 MeV. *Phys. Rev. C*, **49**:3128–3136, 1994. http://prc.aps.org/abstract/PRC/v49/i6/p3128_1.

[45] T. Rönnqvist, H. Condé, N. Olsson, E. Ramström, R. Zorro, J. Blomgren, A. Håkansson, A. Ringbom, G. Tibell, O. Jonsson, L. Nilsson, P. U. Renberg, S. Y. van der Werf, W. Unkelbach, and F. P. Brady. The ^{54,56}Fe$(n,p)^{54,56}$Mn reactions at $E_n = 97$ MeV. *Nucl. Phys. A*, **563**:225–246, 1993. http://www.sciencedirect.com/science/article/pii/037594749390603U.

[46] K. Langanke and G. Martínez-Pinedo. Rate Tables for the Weak Processes of pf-SHELL Nuclei in Stellar Environments. *Atomic Data and Nuclear Data Tables*, **79**:1–46, 2001. http://www.sciencedirect.com/science/article/pii/S0092640X01908654.